Downloaded from orbit.dtu.dk on: Mar 18, 2025

DTU Library

Experimental investigation of the impact of compound-specific dispersion and electrostatic interactions on transient transport and solute breakthrough

Muniruzzaman, Muhammad; Rolle, Massimo

Published in:
Water Resources Research

Link to article, DOI:
10.1002/2016WR019727

Publication date:
2017

Document Version
Peer reviewed version

Link back to DTU Orbit

Citation (APA):
Muniruzzaman, M., & Rolle, M. (2017). Experimental investigation of the impact of compound-specific dispersion and electrostatic interactions on transient transport and solute breakthrough. *Water Resources Research*, *53*(2), 1189-1209. https://doi.org/10.1002/2016WR019727

General rights
Copyright and moral rights for the publications made accessible in the public portal are retained by the authors and/or other copyright owners and it is a condition of accessing publications that users recognise and abide by the legal requirements associated with these rights.

- Users may download and print one copy of any publication from the public portal for the purpose of private study or research.
- You may not further distribute the material or use it for any profit-making activity or commercial gain
- You may freely distribute the URL identifying the publication in the public portal

If you believe that this document breaches copyright please contact us providing details, and we will remove access to the work immediately and investigate your claim.

This is a Post Print of the article published on line 13th January 2017 in Water Resources Research. The publishers' version is available at the permanent link: doi: 10.1002/2016WR019727

Experimental investigation of the impact of compound-specific dispersion and electrostatic interactions on transient transport and solute breakthrough

Muhammad Muniruzzaman[1] and Massimo Rolle* [1,2]

[1]Center for Applied Geosciences, University of Tübingen, Hölderlinstr. 12, D-72074 Tübingen, Germany

[2]Department of Environmental Engineering, Technical University of Denmark, Miljøvej, Building 115, 2800 Kgs. Lyngby, Denmark

*Corresponding author phone: +45 45251566; email: masro@env.dtu.dk

Highlights

- Investigation of 2-D transient transport with high-resolution multitracer and multicomponent ionic flow-through experiments
- Distinct breakthrough curves of different conservative solutes in strongly advection-dominated flows
- Both spreading and mixing depend on tracer diffusion and charge-induced Coulombic interactions

ABSTRACT

This study investigates the effects of compound-specific diffusion/dispersion and electrochemical migration on transient solute transport in saturated porous media. We conducted laboratory bench-scale experiments, under advection-dominated regimes (seepage velocity: 0.5, 5, 25 m/day), in a quasi two-dimensional flow-through setup using pulse injection of multiple tracers (both uncharged and ionic species). Extensive sampling and measurement of solutes' concentrations (~1500 samples; >3000 measurements) were performed at the outlet of the flow-through setup, at high spatial and temporal resolution. The experimental results show that compound-specific effects and charge-induced Coulombic interactions are important not only at low velocities and/or for steady-state plumes but also for transient transport under high flow velocities. Such effects can lead to a remarkably different behavior of measured breakthrough curves also at very high Péclet numbers. To quantitatively interpret the experimental results, we used four modeling approaches: classical advection-dispersion equation (ADE), continuous time random walk (CTRW), dual domain mass transfer model (DDMT), and a multicomponent ionic dispersion model. The latter is based on the multicomponent formulation of coupled diffusive/dispersive fluxes and was used to describe and explain the electrostatic effects of charged species. Furthermore, we determined experimentally the temporal profiles of the flux-related dilution index. This metric of mixing, used in connection with the traditional solute breakthrough curves, proved to be useful to correctly distinguish between plume spreading and mixing, particularly for the cases in which the sole analysis of integrated concentration breakthrough curves may lead to erroneous interpretation of plume dilution.

1. INTRODUCTION

Conservative transport in porous media is determined by fundamental physical (e.g., aqueous diffusion, advection) and/or electrochemical (e.g., Coulombic effects, ion-pairing, charge coupling) processes [e.g., *Gvirtzman and Gorelick*, 1991; *Kitanidis*, 1994; *Haggerty and Gorelick*, 1995, *Boudreau*, 1997; *Thullner et al.*, 2005; *Appelo and Wersin*, 2007; *Steefel and Maher*, 2009]. Dilution and mixing are among the most important mechanisms controlling solute transport in porous media [e.g., *Dentz et al*. 2011; *Le Borgne et al*., 2011]. In particular, these mechanisms are ultimately controlled by small-scale processes such as diffusion and local scale dispersion [e.g., *Chiogna et al.*, 2011; *Cirpka et al.*, 2011]. Numerous studies focusing on experimental and numerical investigations have contributed to the increased recognition that aqueous diffusion, which is the only true mixing process in groundwater [*Kitanidis*, 1994], quantitatively plays an important role on macroscale solute transport in porous media [e.g., *Carrera et al.*, 1998; *LaBolle and Fogg*, 2001; *Chiogna et al.*, 2010; *Zhang et al.*, 2010; *Fiori et al.*, 2011; *Haberer et al.*, 2011; *Molins et al.*, 2012 *Rolle et al.*, 2013a; *Hadley and Newell*, 2014]. Recent experiments and pore-scale simulations showed the key effects of incomplete mixing in the pore channels on the observed macroscopic transport behavior [e.g., *Raje and Kapoor*, 2000; *Gramling et al.*, 2002; *Tartakovsky et al.*, 2009] and have triggered the development of new transport formulations and modeling approaches [e.g., *Willman et al., 2008; Edery et al.*, 2009; *Sanchez-Vila et al.*, 2010; *Chiogna and Bellin*, 2013; *Porta et al.*, 2015]. Incomplete mixing is due to the slow rate of diffusion, which allows concentration gradients to be sustained at the small scale [*Cao and Kitanidis*, 1998; *Rolle et al*., 2012]. In the study of transverse mixing, such effects were found to be responsible

for the nonlinear dependence of the mechanical dispersion term on the average flow velocity, as well as on its direct dependence on the solute diffusivity also in advection-dominated regimes [e.g., *Chiogna et al.*, 2010; *Rolle et al.*, 2012; *Scheven et al.*, 2013; *Hochstelter et al.*, 2013]. An aspect that has been investigated in the geochemical literature [*Vinograd and McBain*, 1941; *Felmy and Weare*, 1991; *Van Cappellen and Gaillard*, 1996; *Giambalvo et al.*, 2002; *Liu*, 2007; *Appelo et al.*, 2008; *Steefel and Maher*, 2009], but that is not often considered in subsurface hydrology studies is that, besides diffusion, also electrostatic interactions affect the movement of charged solutes (e.g., major ions and many inorganic and organic contaminants) in groundwater. The capability to capture, accurately describe, and properly upscale the effects of controlling small-scale processes on macroscopic transport is of primary importance to further develop and advance the current descriptions and formulations of solute transport in porous media. To this end, controlled laboratory experiments are instrumental to provide high-resolution data necessary to test and validate different modeling approaches. Despite a wealth of experimental data have been collected over decades in laboratory flow-through systems and particularly in 1-D column setups [e.g. *Delgado*, 2006], multidimensional and multi-tracer transient experiments with depth-resolved measurements are rare. Although it might be argued that depth-integrated measurements are more convenient and representative of common practice, they are not ideal to understand transport and mixing processes [*Cirpka and Kitanidis*, 2000]. In particular, if the goal is to characterize the effects of small-scale diffusive processes on transient solute transport, depth-resolved measurements of solute concentrations (and volumetric fluxes) are necessary.

The main objective of this study is to provide a detailed experimental investigation of transient transport in saturated porous media and, specifically, to explore the effects of compound-specific and electrostatic interactions. We performed laboratory bench-scale experiments in homogeneously packed quasi 2-D setups under advection-dominated regimes. In particular, we simultaneously injected multiple tracers (both "charge-neutral" and "charged" species) to identify the effects of compound-specific diffusion/dispersion, pore-scale incomplete mixing, and electrostatic interactions on plume dilution and spreading. The injection of a small pulse facilitates establishing "fully 2-D" transient plumes that mix with the surrounding water. The plumes' breakthrough at the outlet was measured at high spatial and temporal resolution. Such sampling approach allows characterizing both longitudinal and transverse evolution of the tracers' plumes. We determined experimentally an entropy-based metric of mixing, the flux-related dilution index, from concentrations and flow rates measurements. Temporal profiles of this quantity were helpful for the interpretation of the integrated flux-weighted breakthrough curves and to help distinguishing between plume spreading and dilution. The concentration breakthrough curves were quantitatively analyzed with different transport models: classical advection-dispersion model (ADE), continuous time random walk (CTRW), and dual-domain mass transfer model (DDMT). The electrostatic behavior of multicomponent ionic tracers was explained by using a forward model based on a Nernst-Planck formulation including the coupling of dispersive fluxes. Both experimental and model outcomes show that the aqueous diffusion and the electrostatic interactions can significantly impact the macroscale transient transport and can lead to remarkably different behaviors under strongly advection-dominated regimes. Our experimental

dataset also represents a challenge, as well as an opportunity of further development, for the different solute transport models. In fact, despite individual fits could reproduce the measured concentrations, generalized formulations able to consistently capture all experimental conditions will need to be developed.

2. EXPERIMENTAL SETUP

Laboratory experiments were performed to investigate transient solute transport, as well as plume dilution in a quasi 2-D flow-through system. The experimental setup consists of an acrylic-glass chamber which has inner dimensions of 100 cm × 19 cm × 1 cm (L × H × W). The flow-through chamber is equipped with 24 equally-spaced (5 mm spacing) ports at both inlet and outlet ends (Figure 1). At each end, these injection (inlet) and extraction (outlet) ports are directly connected to a 24-channel high-precision peristatic pump (ISMATEC IPC-N24, Ismatec, Glattburg, Switzerland) through Fluran HCA pump tubings (ID 0.64 mm; Ismatec, Glattburg, Switzerland). The flow-through setup was homogeneously packed with glass beads with a grain size diameter of 1.00-1.50 mm (Sartorius AG, Göttingen, Germany). In order to avoid possible air entrapment in the water-saturated porous medium, a wet-packing procedure was followed in the packing step [e.g., *Haberer et al*., 2012]. The peristaltic pumps were used to obtain a uniform horizontal fluid flow in the porous medium. Before each experiment, both inlet and outlet pumps were calibrated and the experiments were performed in a temperature controlled room (T = 20 °C). Figure 1 illustrates the experimental setup, as well as an example of high-resolution sampling at the outlet ports.

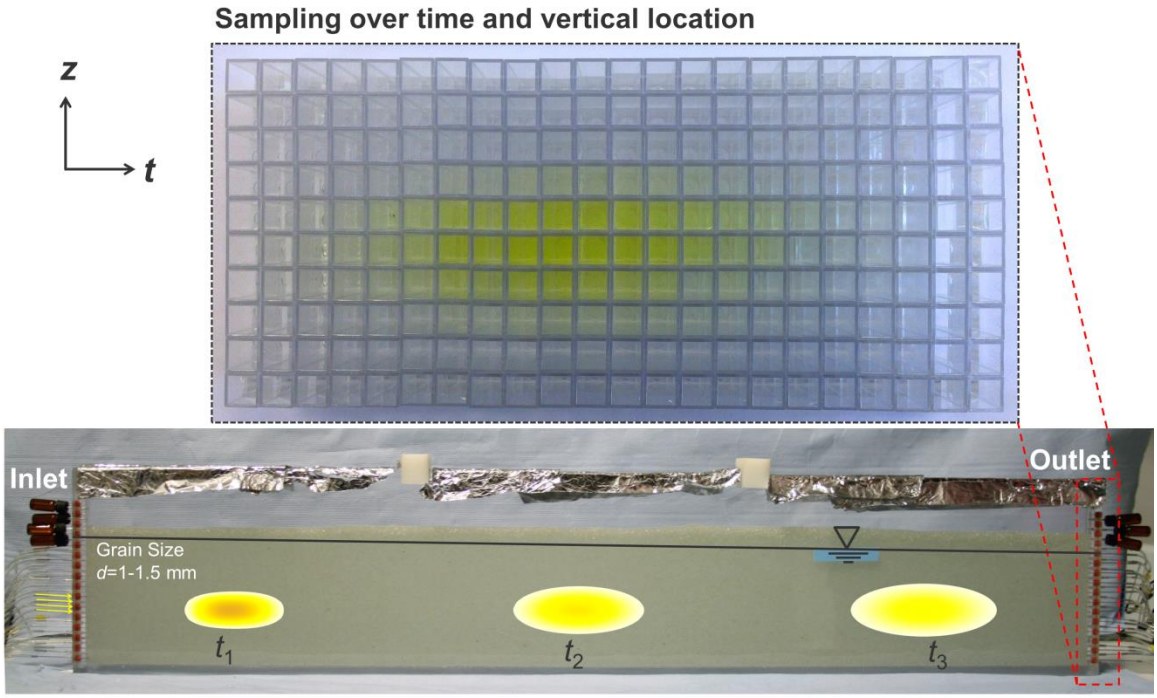

Figure 1. Laboratory flow-through setup with the schematic illustration of the temporal evolution of a tracer plume injected from the four central inlet ports. The inset shows a photograph of fluorescein samples collected at different vertical locations at the outlet as a function of time.

The experiments were initiated by establishing a steady water flow by flushing the domain with at least two pore volumes. When the flow-condition was completely stable over time, we started the transport experiments by injecting the tracer solutions through the four central inlet ports (port number 10, 11, 12 and 13; corresponding to the vertical locations of 5, 5.5, 6 and 6.5 cm from the bottom of the chamber, respectively). All tracer experiments were performed by applying a pulse input at the inlet boundary for a finite duration. To ensure similar injection conditions in the different experiments, we inject the tracer solutions for the duration of ~0.05 pore volumes. Afterwards, samples were taken at all the outlet extraction ports at regular time intervals. Such sampling strategy allowed

us to measure high-resolution temporal and spatial profiles at the outlet of the flow-through system. Additionally, we determined the volumetric water flux in each extraction port by collecting and weighing the effluent for a given period of time. Details of the experimental settings are reported in Table 1.

Table 1. Summary of geometry and transport parameters of the experimental system

Experimental settings	
Flow-through chamber dimensions (L×H×W) [cm]	100×19×1
Number of inlet/outlet ports used	23/24
Port spacing [mm]	5
Grain diameter of porous matrix [mm]	1.00-1.50
Seepage velocity [m/day]	0.5, 5, 25
Average porosity [-]	0.41
Diffusion coefficients	D_{aq} [m^2/s][a]
Na^+	1.20×10^{-9}
K^+	1.77×10^{-9}
Mg^{2+}	0.63×10^{-9}
Cl^-	1.81×10^{-9}
Br^-	1.86×10^{-9}
Fluorescein[b]	0.45×10^{-9}

[a] values from *Lasaga* [1998] at 18°C, and corrected for temperature and viscosity changes at 20°C (experimental conditions)
[b] calculated after *Worch* [1993]

In this work, we performed two types of experiments to explore the behavior of different tracers: (i) multi-tracer experiments, and (ii) multicomponent ionic experiments. Multi-tracer experiments were conducted at three distinct nominal seepage velocities of 0.5, 5 and 25 m/day. Solutions containing potassium chloride (30-136 mg/L) and sodium fluorescein (27-102 mg/L) were used as tracer solutions; whereas ultra-pure Milli-Q water (Labostar 1-DI, Evoqua, USA) was used as background solution. The aqueous diffusivities of the different solutes vary considerably and are reported in Table 1. Multicomponent ionic experiments were performed to show the relevance of electrostatic

effects during transient transport in multi-ionic environments. In these experiments, a pulse of 1:2 electrolyte solution (magnesium chloride; 0.80 mM) was injected into the saturated porous medium. As background solution, either Milli-Q water or NaBr solution (1:1 electrolyte; 4.04 mM) was used for these experiments (Table 2). The multicomponent ionic experiments were performed at a flow velocity of ~5 m/day.

The samples collected at the outlet ports were analyzed to determine the concentration of the different solutes. Fluorescein concentration was measured by using a UV-spectrophotometer (DR 2800, Hach, Germany). The extinction and emission wavelengths were 483 and 515 nm, respectively. The anion concentrations (Cl^-, Br^-) were measured by ion-chromatography (Dionex ICS-1500, Thermo Scientific, USA); whereas the cations (Mg^{2+} and Na^+) were measured by ICP-MS (Agilent 7700 Series, Agilent Technologies, Japan). Table 2 summarizes important experimental conditions, as well as details on the sampling procedure.

Table 2. Tracers' inlet concentrations, pulse duration, sampling intervals and number of samples

Experiments	**Tracer concentrations**		**Pulse duration [min]**	**Sampling intervals [min]**	**No. of Samples**	**No. of Measure-ments**
Multi-tracer experiments						
	Fluorescein [mg/L]	*KCl [mg/L]*				
$v \approx 0.5$ m/day (Pe_{Cl^-}=4, Pe_{Fluor}=16)	27	30	165	50	260	520
$v \approx 5$ m/day (Pe_{Cl^-}=40, Pe_{Fluor}=161)	101.6	136.2	15	5	300	600
$v \approx 25$ m/day (Pe_{Cl^-}=200, Pe_{Fluor}=804)	35.9	40.7	3	1	270	540
Multicomponent ionic experiments ($v \approx 5$ *m/day*)						
	Tracer ($MgCl_2$)	*Background Solution*				
(a) in pure water	0.80 mM	Milli-Q water	15	5	300	600
(b) in a buffer electrolyte solution	0.80 mM	NaBr (4.04 mM)	15	5	300	1200

3. MODELING APPROACH AND DATA EVALUATION

Four different solute transport models were used to interpret the results of the multi-tracer experiments. This section summarizes the main equations of these models and the data evaluation approaches. Further details about the different models are provided in the Supporting Information.

3.1 Analysis of Breakthrough Curves (BTC)

3.1.1 Advection-Dispersion Equation (ADE)

The analytical solution of the 2-D advection-dispersion equation, subjected to a pulse input of the tracer along a line source for a finite duration, is given by [e.g., *Leij et al*., 1991; *van Genuchten et al*., 2013]:

$$C(x,z,t) = \frac{C_0}{2} \int_{P(t)}^{t} \frac{x}{\tau}\left[\left\{\frac{1}{\sqrt{4\pi D_L \tau}}\exp\left(-\frac{(x-v\tau)^2}{4D_L\tau}\right)\right\}\cdot\left\{erfc\left(\frac{z-w/2}{\sqrt{4D_T\tau}}\right)-erfc\left(\frac{z+w/2}{\sqrt{4D_T\tau}}\right)\right\}\right]d\tau$$

where, (1)

$$P(t)=\begin{cases} 0 & \text{when} \quad 0 < t \le t_0 \\ t-t_0 & \text{when} \quad t > t_0 \end{cases}$$

where C [M/L^3] is the concentration of the solute, v [L/T] is the seepage velocity, D_L [L^2/T] and D_T [L^2/T] are longitudinal and transverse hydrodynamic dispersion coefficients, respectively, x [L] and z [L] are the spatial coordinates in the directions parallel and orthogonal to the principal flow direction, and t [T] denotes the time. w [L] denotes the source width at the inflow, C_0 [M/L^3] is the inflow concentration, and t_0 [T] is the duration of the pulse.

For the analysis of breakthrough curves a 1-D model is convenient and it becomes necessary when only vertically integrated measurements are available. The analytical solution for 1-D transport problem for the equivalent boundary and initial conditions reads as [e.g., *van Genuchten et al*., 2013]:

$$C(x,t) = \frac{C_0}{2}\left[\left\{erfc\left(\frac{x-vt}{\sqrt{4D_L t}}\right) - erfc\left(\frac{x-v(t-t_0)}{\sqrt{4D_L(t-t_0)}}\right)\right\} + \exp\left(\frac{vx}{D_L}\right)\left\{erfc\left(\frac{x+vt}{\sqrt{4D_L t}}\right) - erfc\left(\frac{x+v(t-t_0)}{\sqrt{4D_L(t-t_0)}}\right)\right\}\right] \quad (2)$$

This simplified 1-D analytical solution agrees very well with the full 2-D analytical solution of equation (1) when the mass-fluxes at a specific cross-section are vertically integrated and normalized by the integrated mass-flux at the inflow boundary (Figure S1). We denote this spatially integrated quantities as "boundary-normalized integrated breakthrough curves" or, for simplicity, just "integrated BTCs" $\left(\hat{C}(x,t)\Big|_{BN}^{BTC}\right)$:

$$\hat{C}(x,t)\Big|_{BN}^{BTC} = \frac{\int_{-\infty}^{\infty} C(x,z,t)q_x(z)dz}{\int_{-\infty}^{\infty} g(z,t)q_x(z)dz} \quad (3)$$

where q_x [L/T] is the specific discharge in the longitudinal direction. We used this 1-D solution (equation (2)) to fit the breakthrough curves measured at each individual outlet ports (local BTC), as well as the integrated BTCs (equation (3)).

3.1.2 Non-Fickian Transport Models

In order to investigate the "non-Fickian" or "anomalous" behavior of tracer plumes studied in our experiments, we used continuous time random walk (CTRW) and dual

194 domain mass transfer model (DDMT). The CTRW transport equation in partial
195 differential equation form reads as [e.g., *Berkowitz et al.*, 2006; *Berkowitz and Scher*,
196 2009; *Heidari and Li*, 2014]:

$$\frac{\partial c(\mathbf{s},t)}{\partial t} = -\int_0^t M(t-t')\left[\mathbf{v}_\psi \cdot \nabla c(\mathbf{s},t') - \mathbf{D}_\psi : \nabla\nabla c(\mathbf{s},t')\right]dt' \tag{4}$$

197 in which $c(\mathbf{s}, t)$ is the concentration, $\mathbf{v}_\psi$ and $\mathbf{D}_\psi$ are the transport velocity and generalized
198 dispersion coefficient, respectively. $M(t)$ is a memory function which accounts for the
199 unknown, small-scale heterogeneities beyond the level of experimental detection [*Cortis*
200 *and Berkowitz*, 2005; *Kosakowski et al.*, 2001]. This memory function can take any
201 possible form depending on the functional form of probability rate for transition time
202 ($\tilde{\psi}(u)$).The truncated power law (TPL) form of $\tilde{\psi}(u)$ is written as:

$$\tilde{\psi}(u) \equiv (1+\tau_2 u t_1)^\beta \exp(t_1 u)\frac{\mathbf{\Gamma}\left(-\beta, \tau_2^{-1} + t_1 u\right)}{\mathbf{\Gamma}\left(-\beta, \tau_2^{-1}\right)} \qquad 0 < \beta < 2 \tag{5}$$

203 where t_1 and t_2 (with $\tau_2 \equiv t_2/t_1$) are the lower and upper limits of power law behavior
204 respectively, u is the Laplace variable, and $\mathbf{\Gamma}$ is incomplete gamma function. β is a
205 measure of the extent of "non-Fickian" or "anomalous" nature of transport with values
206 between 0 and 2 representing the non-Fickian behavior.
207
208 The transport equations for DDMT for a first-order exchange in 1-D domain are given by
209 [e.g., *van Genuchten and Wierenga*, 1976; *Valocchi*, 1985; *Gorelick et al*., 2005; *Luo et*
210 *al. 2005 and 2007*]:

$$\eta_m \frac{\partial C_m}{\partial t} + \eta_{im} \frac{\partial C_{im}}{\partial t} + q\frac{\partial C_m}{\partial x} - \eta_m \frac{\partial}{\partial x}\left(D_L^m \frac{\partial C_m}{\partial x}\right) = 0 \tag{6}$$

$$\eta_{im} \frac{\partial C_{im}}{\partial t} = \xi\left(C_m - C_{im}\right) \tag{7}$$

where the indices *m* and *im* refer to the mobile and immobile domains, respectively. C_m [M/L^3] and C_{im} [M/L^3] are the concentrations in mobile and immobile domain; η_m [-] and η_{im} [-] are the mobile and immobile porosities, respectively; q [L/T] denotes the specific discharge; and ξ [1/T] is the mass transfer coefficient.

3.1.3 Optimization Procedure

In order to fit the different models to the experimental data, the following objective function was considered:

$$\chi^2 = \sum_{i=1}^{N_{meas}} \left(C_i^{meas} - C_i^{mod}\right)^2 \tag{8}$$

where N_{meas} is the number of data points, C_i^{meas} is the normalized measured concentrations, and C_i^{mod} is the normalized model predicted concentrations. For the fitting of breakthrough curves with the ADE model, seepage velocity (v) and dispersion coefficient (D_L) were considered as fitting parameters. In CTRW fitting, we considered both transport parameters (v_ψ, D_ψ) as well as TPL functional parameters (β, t_1, t_2) as fitting parameters. The fitting parameters in DDMT model were mobile transport coefficients (v_m, D_m), mobile porosity (η_m), and mass transfer coefficient (ξ). The latter two models contain more fitting parameters compared to ADE and offer more flexibility to obtain a better fit to the data, in particular when "anomalous" transport features characterize the solutes' breakthrough. The minimization of non-linear least squares problems was performed with the MATLAB function *lsqnonlin* using a trust-region reflective algorithm [e.g., *Coleman and Li*, 1996].

231 **3.2 Quantification of Transverse Dispersion**

232 In order to quantify the transverse displacement of the injected plumes in our quasi 2-D
233 flow-through systems, we match the experimentally measured concentrations with the
234 ADE model to obtain transverse dispersion coefficient, D_T. This can be done by fitting
235 the 2-D analytical solution of equation (1) with the locally measured breakthrough curves
236 at all individual outlet ports. Alternatively, following a similar approach to the one
237 described in equation (3), we can further simplify the treatment by "decoupling" the
238 transverse problem from the longitudinal one. The simplification is done by integrating
239 the outlet concentrations over time at each vertical location. Thus, we consider only the
240 plumes' displacement in the transverse direction. As done in equation (3), these time-
241 integrated concentrations are normalized by the time-integrated inflow boundary
242 condition and we term this quantity as "boundary normalized integrated spatial profiles"
243 or just "integrated spatial profiles" $\left(\hat{C}(x,z)\Big|_{BN}^{SP}\right)$:

$$\hat{C}(x,z)\Big|_{BN}^{SP} = \frac{\int_0^\infty C(x,z,t)dt}{\int_0^\infty g(z,t)dt} \tag{9}$$

244 Along a specific cross-section, the above time-integrated quantity of equation (9)
245 produces the same outcome as the analytical solution for 2-D steady-state transport
246 (Figure S2) with a line source at the inlet [*Domenico and Palciauskas*, 1982]:

$$C(x,z) = \frac{C_0}{2}\left\{erfc\left(\frac{z-w/2}{\sqrt{4D_T x/v}}\right) - erfc\left(\frac{z+w/2}{\sqrt{4D_T x/v}}\right)\right\} \tag{10}$$

Therefore, we fit equation (10) to the time-integrated spatial profiles $\left(\hat{C}(x,z)\Big|_{BN}^{SP}\right)$, calculated from our measured data, to characterize the transverse evolution (D_T) of the injected tracers at the outlet of the domain.

3.3 Evaluation of Plume Dilution

As a metric of dilution, we use the flux-related dilution index. This quantity describes dilution as the "act of distributing a given solute mass flux over a larger water flux" and represents the effective volumetric water flux carrying the solute mass flux at a given longitudinal cross-section [*Rolle et al*., 2009]. For transient transport in porous media, the flux-related dilution index can be written as [*Rolle and Kitanidis*, 2014]:

$$E_Q(x,t) = \exp\left(-\int_{\Omega} p_Q(x,t) \ln p_Q(x,t) q_x(x,t) d\Omega\right) \tag{11}$$

where $q_x = v\theta$ is the longitudinal component of specific discharge, Ω [L^2] is the cross-sectional area perpendicular to the main flow, θ [-] is the total porosity, and p_Q [T/L^3] is the flux-related probability density function at time t:

$$p_Q(x,t) = \frac{C(x,t)}{\int_{\Omega} C(x,t) q_x(x,t)} \tag{12}$$

3.4 Modeling Multicomponent Ionic Dispersion

The transport mechanism of charged solutes in a multi-ionic environment is conceptually different compared to the charge-neutral species due to the additional contribution of electrostatic interactions. Mathematically, transport processes of such charged species are commonly described by the Nernst-Planck formulation, by explicitly accounting for

electrochemical potential gradients [e.g., *Bard and Faulkner*, 2001; *Cussler*, 2009]. For the multicomponent transport of dilute electrolyte solutions under the simplified condition of negligible ionic strength gradients, the total diffusive flux of ionic species is expressed as the additional contribution of a purely diffusive flux (Fick's law) and an electrochemical migration term [e.g., *Lasaga*, 1978; *Boudreau et al*., 2004; *Appelo and Wersin*, 2007]:

$$J_i = -D_i \nabla C_i - D_i \frac{z_i F}{RT} C_i \nabla \Phi \tag{13}$$

where C_i is the concentration of a mobile charged species i (i = 1,2,3,…,N), D_i is the "self-diffusion" coefficient (i.e., diffusion at its "liberated" state), z_i denotes the charge, F is the Faraday's constant, R is the ideal gas constant, T is the temperature, and Φ is the electrostatic potential.

By considering the electroneutrality constraints of the solution: i.e., (i) condition of local charge-balance $\sum_{i=1}^{N} z_i C_i = 0$ and/or (ii) condition of maintaining zero electrical current, $\sum_{i=1}^{N} z_i J_i = 0$, the electrostatic potential gradient $(\nabla \Phi)$ can be expressed as:

$$\nabla \Phi = \frac{\sum_{i=1}^{N} \left(z_i D_i \nabla C_i \right)}{\sum_{i=1}^{N} \left(z_i^2 F D_i C_i \right) / RT} \tag{14}$$

As a result, the flux expression of equation (13) takes the form,

$$J_i = -D_i \nabla C_i + \frac{z_i D_i C_i}{\sum_{j=1}^{N} \left(z_j^2 D_j C_j \right)} \sum_{k=1}^{N} \left(z_k D_k \nabla C_k \right) \tag{15}$$

This formulation enables accounting for both the movements due to the self-diffusion, as well as the concentration gradients of other dissolved charged species. Key steps regarding the detailed derivation of the above equations can be found in the works of *Ben-Yaakov*, 1972; *Lasaga*, 1979, *Van Cappellen and Gaillard*, 1996; *Boudreau et al*., 2004; *Appelo and Wersin*, 2007; *Liu et al*., 2011 among others. Under flow-through conditions, self-diffusion coefficients in equations (13-15) should be replaced by hydrodynamic dispersion coefficients since the transport is also influenced by the fluid flow [e.g., *Rolle et al*., 2013b; *Muniruzzaman and Rolle*, 2015]. Therefore, using the above flux expression, the governing multicomponent transport equation for ionic solutes in 2-D saturated porous media reads as:

$$\frac{\partial C_i}{\partial t} = -v\frac{\partial C_i}{\partial x} + \frac{\partial}{\partial x}\left(\sum_{j=1}^{N}\mathbf{D}_L^{ij}\frac{\partial C_i}{\partial x}\right) + \frac{\partial}{\partial z}\left(\sum_{j=1}^{N}\mathbf{D}_T^{ij}\frac{\partial C_i}{\partial z}\right) \tag{16}$$

in which $\mathbf{D}_L^{ij}$ and $\mathbf{D}_T^{ij}$ are the matrices of longitudinal and transverse cross-coupled dispersion terms [*Muniruzzaman et al*., 2014], respectively. These inter-dispersion coefficients are defined as:

$$\begin{aligned}\mathbf{D}_L^{ij} &= \delta_{ij}D_L^i - \frac{z_i z_j D_L^i D_L^j C_i}{\sum_{k=1}^{N}\left(z_k^2 D_L^k C_k\right)} \\ \mathbf{D}_T^{ij} &= \delta_{ij}D_T^i - \frac{z_i z_j D_T^i D_T^j C_i}{\sum_{k=1}^{N}\left(z_k^2 D_T^k C_k\right)}\end{aligned} \tag{17}$$

with D_L^i and D_T^i being the longitudinal and transverse "self-dispersion coefficient" (i.e., when a particular ion, *i* is "liberated" from the other charged species in solution) and δ_{ij} being the Kronecker delta that is equal to 1 when $i=j$ and equal to 0 if $i\neq j$. The multicomponent ionic transport model is solved using a finite volume scheme (FVM) on

297 streamline-oriented grids with the approach of *Cirpka et al*. [1999a; 1999b]. We use a
298 discretization of Δx = 5 mm and Δz = 1 mm to simulate the outcomes obtained in our
299 multicomponent ionic transport experiments. The simulations are performed using a
300 pulse type boundary at the inlet and zero dispersive flux at the remaining boundaries. In
301 order to linearize the non-linearity induced from the coupled dispersive fluxes in the
302 transport equations (equations (16-17)), we use a Picard iterative scheme to solve the
303 system of equations. The concentration matrix is solved with the direct matrix solver
304 UMFPACK [*Davis and Duff*, 1997] and the calculations are performed in MATLAB®.
305 Further information regarding the development of this multicomponent ionic modeling
306 approach can be found in *Muniruzzaman et al*. [2014] and *Muniruzzaman and Rolle*
307 [2016].
308
309

310 ## 4. RESULTS AND DISCUSSION

311 We performed experiments with two distinct sets of tracers: (i) multi-tracer experiments
312 (with "non-interacting" tracers: fluorescein and chloride), and (ii) multicomponent ionic
313 experiments (with electrostatically interacting $MgCl_2$ solutions in different background
314 solutions).

315 ### 4.1 Multi-tracer Experiments

316 *4.1.1 Integrated Breakthrough Curves*

317 The experiments were performed at three planned nominal seepage velocities of 0.5, 5
318 and 25 m/day. The actual seepage velocities were determined by fitting the measured
319 concentration breakthrough curves with the different models and the results, reported in

320 Table 3, show an overall good agreement with the nominal values although some
321 deviations were observed. In the following discussion, we refer to the experiments using
322 the nominal values of seepage velocity. Specifically, we use the notation $v \approx 0.5$, 5 and 25
323 m/day to distinguish the three different cases. Chloride and fluorescein were used as
324 tracers and measured at the outlet. Chloride has significantly higher (approximately
325 fourfold) diffusivity compared to that of fluorescein (Table 1). Figure 2 summarizes the
326 integrated breakthrough curves (equation (3)) along with the flux-related dilution index
327 (equation (11)) measured in the experiments at different seepage velocities at the outlet of
328 the flow-through setup. The breakthrough of the tracers was observed with no retardation
329 for chloride and with a slight retardation for fluorescein (linear retardation factor of ~1.04)
330 due to weak sorptive interactions with the solid matrix. The breakthrough curves of the
331 two tracers are reported as function of the pore volumes for direct comparison.
332 Examining the temporal trend of the concentration profiles, integrated over the entire
333 cross-section, approximately bell-shaped curves for different velocities can be observed
334 (Figure 2a-c). However, the breakthrough curves for the two different tracers, chloride
335 (black circles) and fluorescein (black crosses), show remarkably different spreading and
336 peak concentrations at all velocities. The curves for chloride (solute with higher
337 diffusivity, $D_{aq} = 1.81\times10^{-9}$ m^2/s) exhibit higher peak concentrations and have less spread
338 profiles than the ones of fluorescein (solute with lower diffusivity, $D_{aq} = 0.45\times10^{-9}$ m^2/s).
339 The lines indicate the best fit modeled curves to the measured concentrations for three
340 different transport models: ADE (red solid lines), CTRW (blue dash-dotted lines), and
341 DDMT (green dashed lines) (Figure 2a-c). Table 3 lists the best fitted parameters
342 obtained from the different models at different velocities. The fitted values of D_L, which

is basically an indicator of the macroscopic spreading of the solute plumes in the longitudinal direction, also show consistent outcomes where longitudinal dispersion of fluorescein is approximately double compared to the ones of chloride in all experiments. Such separations in tracers' concentration profiles and spreading are quite remarkable especially for the cases with very high velocities ($v \approx 5$ and 25 m/day), where transport is strongly advection-dominated.

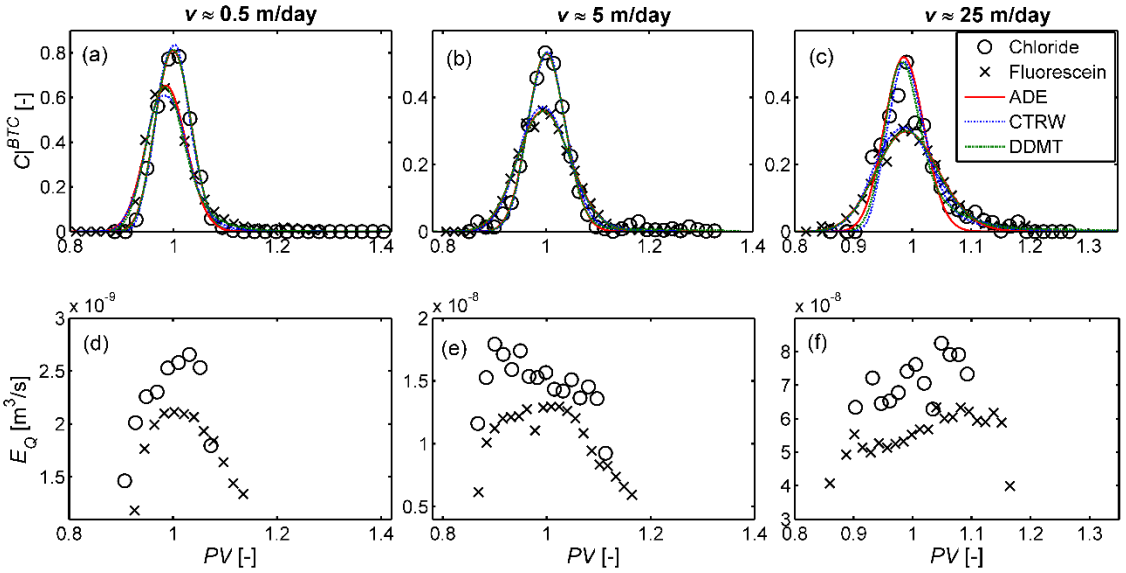

Figure 2. Breakthrough curves of the flux-weighted integrated concentrations, normalized by the flux-weighted inflow boundary conditions (a-c), and flux-related dilution index (d-f) at the outlet cross-section for the seepage velocities of 0.5 m/day (a,d), 5 m/day (b,e) and 25 m/day (c,f).

Although, the compound-specific trends in these solute profiles are quite evident, the observed patterns show that the compound with higher diffusion coefficient (chloride) results in the less spread profile with significantly higher peak concentration compared to the compound with lower diffusivity (fluorescein). This behavior may appear counterintuitive and, based on the exclusive analysis of these integrated breakthrough

curves, one may come to the erroneous conclusion that the more spread and less peaked fluorescein profiles correspond to the more diluted plumes. A similar behavior was observed in the pore-scale modeling study of *Rolle and Kitanidis* [2014], who argued that this behavior is due to the fact that, in advection-dominated regimes, the transport departs from being close to physical equilibrium and spreading ceases to be a good proxy for plume dilution and mixing. This was the case in all experimental setups, in fact, even the experiment with the lowest seepage velocity ($v \approx 0.5$ m/day), which lies in the upper limit of typical natural groundwater flow, is characterized by a grain Péclet number of ~4.96 for chloride and ~19.76 for fluorescein. A metric such as the flux-related dilution index is helpful to distinguish spreading and mixing from the outlet measurements. We computed the flux-related dilution index of the tracer plumes at the outlet at different time points by using the concentrations and volumetric fluxes measured at each individual outlet port (equation (11)). The results show a different pattern compared to the concentration breakthrough curves and suggest that the chloride (tracer with higher D_{aq}) plume is remarkably more diluted compared to fluorescein plume at all velocities (Figure 2d-f). Therefore, despite the more spread integrated breakthrough curves, the water fluxes carrying the fluorescein plumes are, in fact, ~40%, ~33%, and ~20% smaller compared to the ones transporting the chloride plume at the flow velocity of 0.5, 5, and 25 m/day, respectively. The fact that the chloride plumes are more diluted than those of fluorescein directly stems from the higher diffusivity of chloride. Consequently, even though the different tracer pulses were simultaneously injected in the macroscopically homogeneous domain, the tracer compounds evolve differently through the pore-channels because of the different diffusivity and the different extent of incomplete mixing in the pores at these

383 high flow velocities. The macroscopic result of these small scale processes is that the
384 solute with higher diffusivity is distributed over larger volumes and water fluxes. Notice
385 that, although rather intuitive, these results cannot be explained by classical dispersion
386 theory using the common linear parameterization, $D = D_P + \alpha v$ [*Scheidegger*, 1961].
387 According to this parameterization, diffusion only acts through the velocity-independent
388 pore diffusion term (D_P) and, thus, should only play a minor or negligible role in
389 advection- and strongly advection-dominated regimes. Therefore, in contrast to what was
390 observed in the experiments, the same distribution of different solutes at high flow
391 velocity would be expected, due to the fact that in these conditions the mechanical
392 dispersion term dominates. The latter term is described as the product of the seepage
393 velocity and a dispersivity coefficient (α), typically assumed to be a property of the
394 porous medium.
395 The trends of E_Q (x,t) profiles for different solutes at the outlet are also quite interesting
396 (Figure 2d-f). Instead of a monotonically increasing pattern as expected from a Gaussian
397 plume, the dilution profiles have a tendency to either level off or decrease after the mean
398 arrival time. *Rolle and Kitanidis* [2014] observed a similar behavior in pore-scale
399 simulations and pointed out that this effect is determined by two competing factors: the
400 tendency of increasing dilution with travel time and/or travel distance, and the
401 incomplete-mixing at the pore-scale resulting in mass transfer limitations occurring at
402 these rather high flow velocities leading to an effect of "undiluteness" for the different
403 solute plumes. The absolute values of flux-related dilution indices (E_Q) also increase with
404 increasing average seepage velocity (Figure 2d-f). The incomplete mixing and
405 "undiluteness" effect is also visible in the concentration breakthrough curves, especially

406 at high flow velocities ($v \approx 5$ and 25 m/day), with the presence of a tailing at late times
407 (Figure 2b-d). Such effects are indicative of "non-Fickian" or "anomalous" transport
408 behavior. As an example, this behavior is illustrated in Figure 3 by plotting the
409 concentration profiles of the experiment at $v \approx 25$ m/day in log-scale in order to
410 specifically focus on the long-term tailings. In the logarithmic plots it is evident that both
411 tracer compounds show considerable extent of tailing where the ADE model (red solid
412 lines) shows deviation from the data (Figure 3a-b). On the other hand, the CTRW (blue
413 dashed-dotted lines) and the DDMT (green dashed lines) model are able to effectively
414 capture the plume tails. The residuals between the data points and the best fitted modeled
415 values, weighted by the measured values, also confirm consistent outcomes where both
416 CTRW (blue crosses) and DDMT (green squares) model show smaller magnitudes of the
417 weighted residuals at late times (Figure 3c-d). This feature evidently indicates the better
418 performance of these two models over the ADE model (red circles) in reproducing the
419 late-time behaviors (PV>1.1) for both tracer plumes. The characteristics of anomalous
420 nature of the transport are also appreciable from the fitted parameters obtained from the
421 CTRW and DDMT models (Table 3).

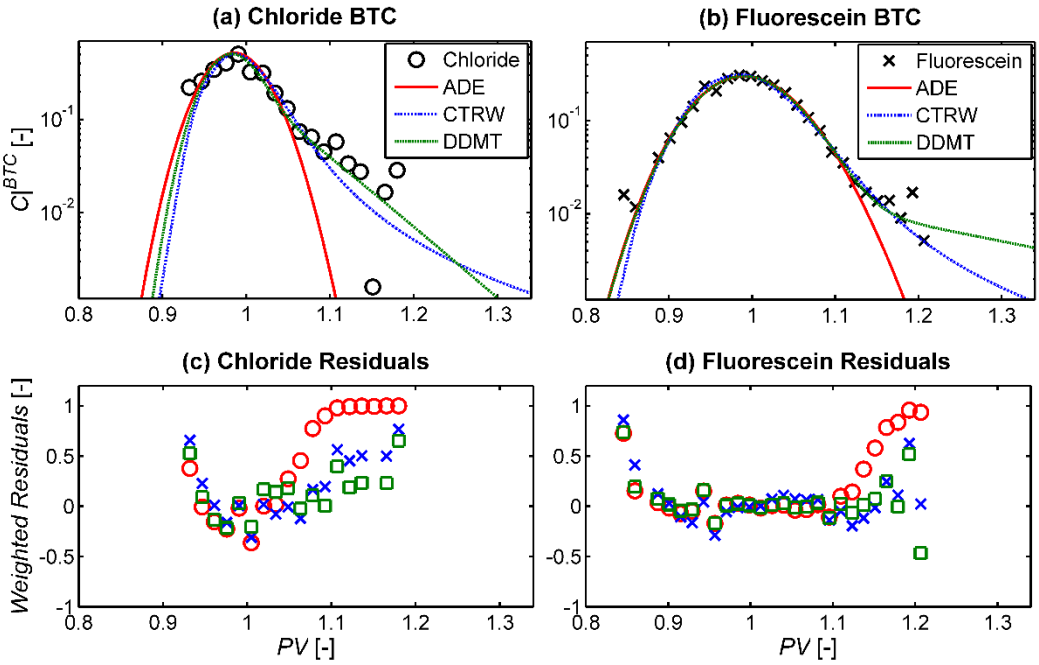

422

423 **Figure 3.** Breakthrough curves of the flux-weighted integrated concentrations normalized
424 by the flux-weighted inflow boundary conditions in logarithmic scale (a,b), and the
425 weighted residuals (c,d) at the seepage velocity of 25 m/day.
426

Table 3: Summary of the fitted parameters for the breakthrough curves integrated over the outlet cross-section

Model	Parameters	$v \approx 0.5$ m/day				$v \approx 5$ m/day				$v \approx 25$ m/day			
		Chloride		Flourescein		Chloride		Flourescein		Chloride		Flourescein	
		Best fit (p)	Std. dev. (σ_p)	Best fit (p)	Std. dev. (σ_p)	Best fit (p)	Std. dev. (σ_p)	Best fit (p)	Std. dev. (σ_p)	Best fit (p)	Std. dev. (σ_p)	Best fit (p)	Std. dev. (σ_p)
ADE	v [m/day]	0.62	3.80×10^{-4}	0.57	4.66×10^{-4}	4.83	2.77×10^{-3}	4.60	2.32×10^{-3}	21.78	2.62×10^{-2}	20.57	1.76×10^{-2}
	D_L [m^2/s]	2.64×10^{-9}	1.23×10^{-10}	4.04×10^{-9}	1.69×10^{-9}	3.21×10^{-8}	8.92×10^{-10}	6.86×10^{-8}	9.54×10^{-10}	1.30×10^{-7}	8.18×10^{-9}	3.44×10^{-7}	7.88×10^{-9}
	D_T [m^2/s]	2.16×10^{-9}	3.41×10^{-10}	9.19×10^{-10}	3.66×10^{-11}	6.67×10^{-9}	2.97×10^{-10}	3.45×10^{-9}	1.50×10^{-10}	1.74×10^{-8}	8.27×10^{-10}	1.10×10^{-8}	6.44×10^{-10}
CTRW	v_ψ [m/day]	0.45	6.78×10^{-9}	0.73	4.46×10^{-6}	4.78	3.52×10^{-5}	4.79	2.24×10^{-4}	38.88	5.16E-04	26.64	1.49×10^{-3}
	D_ψ [m^2/s]	2.76×10^{-10}	1.23×10^{-13}	2.57×10^{-9}	5.22×10^{-11}	1.60×10^{-8}	1.91×10^{-10}	4.37×10^{-8}	3.43×10^{-10}	1.83×10^{-8}	1.01×10^{-9}	1.69×10^{-7}	2.14×10^{-9}
	β [-]	2.364	4.40×10^{-10}	1.781	2.08×10^{-8}	2.006	2.15×10^{-9}	1.957	4.29×10^{-9}	1.549	5.18×10^{-7}	1.768	7.31×10^{-8}
	t_1 [min]	4.38×10^{-1}	7.34×10^{-9}	7.90×10^{-2}	2.96×10^{-9}	2.20×10^{-2}	3.70×10^{-10}	2.43×10^{-2}	6.20×10^{-10}	6.92×10^{-4}	4.8×10^{-9}	6.28×10^{-3}	5.88×10^{-9}
	t_2 [min]	9.16×10^{7}	0.13	7.53×10^{9}	243.12	1.81×10^{8}	1.94	1.41×10^{8}	25.15	1.41×10^{8}	292.98	1.41×10^{8}	14.467
DDMT	v_m [m/day]	0.62	0.0005	0.58	0.0005	4.84	0.0039	4.60	0.0730	21.95	0.02226	20.61	0.1755
	D_m [m^2/s]	2.23×10^{-9}	4.10×10^{-10}	2.74×10^{-9}	4.34×10^{-10}	3.03×10^{-8}	9.21×10^{-10}	6.77×10^{-8}	1.36×10^{-9}	8.08×10^{-8}	1.18×10^{-8}	3.21×10^{-7}	1.08×10^{-8}
	η_m [-]	0.4070	0.0020	0.4038	0.0011	0.4056	0.0002	0.4034	0.0063	0.4015	0.0006	0.4018	0.0031
	ξ [1/s]	2.46×10^{-6}	3.61×10^{-6}	1.16×10^{-6}	2.97×10^{-7}	1.25×10^{-6}	1.64×10^{-8}	4.77×10^{-7}	9.47×10^{-8}	4.37×10^{-5}	6.24×10^{-6}	8.20×10^{-6}	4.76×10^{-7}

Figure 4 shows selected parameters for each model that were obtained from the fitting with experimental data. Panel a summarizes the longitudinal dispersion coefficients (D_L) estimated with the ADE model. The results show distinct values for fluorescein and chloride at all three seepage velocities. The experimentally determined D_L values, represented in a normalized plot (D_L/D_{aq} vs. *Pe*), appear to follow a linear or weakly nonlinear trend that appears to be captured by previously proposed correlations for longitudinal dispersion in porous media [e.g., *Bijeljic et al*., 2004; *Guedes de Carvalho and Delgado*, 2005] (Figure 4b). In CTRW, β is the parameter that determines the extent of anomalous transport with $0<\beta<2$ indicating the existence of non-Fickian behavior. For $\beta>2$, the transport reduces to classical Fickian form. For $v \approx 0.5$ and 5 m/day, the best-fit β values for chloride are 2.364 and 2.006, respectively; whereas for fluorescein the obtained values of β are 1.781 and 1.957, respectively (Figure 4c, Table 3). These values suggest that, while the chloride transport stays in the Fickian regime, the transport of fluorescein becomes "weakly" anomalous even in this homogeneously packed quasi 2-D flow-through setup. These values and their interpretation appear to be reasonable also with respect to the fundamental physical processes in the pore channels and with the compound-specific behavior resulting in fluorescein (lower diffusivity) being relatively more influenced by the incomplete-mixing in the pores than chloride (higher diffusivity). Conversely, at the highest velocity tested ($v \approx 25$ m/day), a $\beta<2$ is obtained for both tracer compounds demonstrating that at such high advective velocity both tracers show anomalous behavior.

The parameters obtained by fitting the DDMT model can also be used to explain the observed behavior of the different tracer plumes (Table 3). For the first two experiments

($v \approx 0.5$ and 5 m/day), the fitted mobile fraction (η_m) of total porosity (θ=0.41) for chloride is slightly higher compared to the values obtained for fluorescein. On the other hand, practically identical results were obtained for the experiments at the highest Péclet number ($v \approx 25$ m/day). As observed for the ADE and the CTRW models, also for the DDMT non-unique and compound-specific fitting parameters were obtained at the different flow velocities. In particular, the higher mass-transfer coefficients obtained for chloride can be related to the higher diffusivity of this species (Figure 4d).

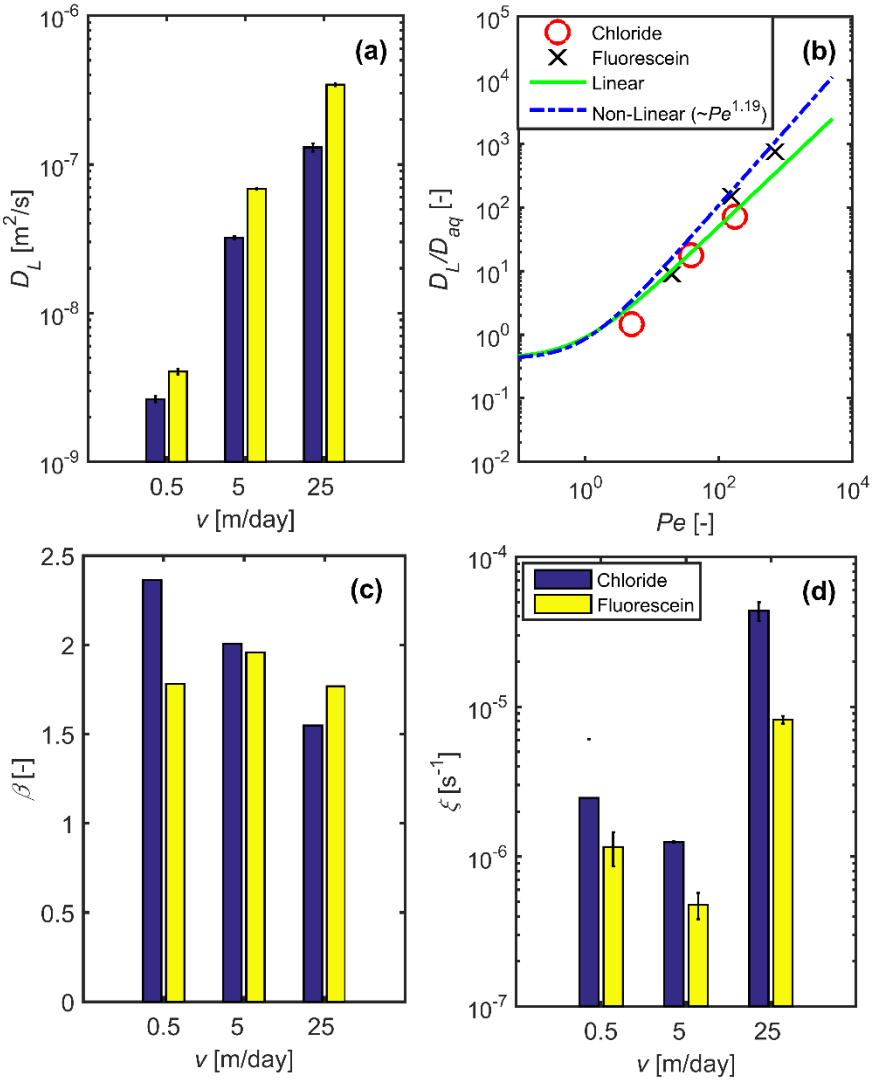

Figure 4. Selected fitted parameters obtained from the integrated breakthrough curves using different models: D_L for ADE (a-b), β for CTRW (c), and ξ for DDMT (d) model.

462 *4.1.2 Port-resolved Breakthrough Curves*

463 Figure 5 depicts the maps of the concentration measurements performed at different
464 locations along the outlet of our 2-D experimental domain at different times. The
465 measurements are shown as concentrations normalized by the corresponding inlet
466 concentrations for each tracer. The top two rows of panels denote the measured data
467 points plotted with vertical locations (z) and data collection time (PV) for different
468 velocities (Figure 5a-f). Each grid block in these plots indicates a measurement point
469 across the time and space; whereas the respective concentration value is shown with the
470 color. The lower two rows of panels represent the cubic interpolation of the measured
471 concentration values (Figure 5g-l). The white dots delineate the contours of the
472 interpolated normalized concentrations, whereas the solid lines represent the
473 corresponding ADE predicted contours shown at levels 0.02 and 0.1. This representation
474 helps visualizing the overall shape of the tracer plumes arriving at the outlet cross-section.
475 In fact, assuming a macroscopically homogeneous domain and a constant advective
476 velocity, the time axis can be translated into space with $x = vt$. So, these concentration
477 distributions can be viewed as analogous to a snapshot of the spatial distribution of the
478 tracer plume at the mean breakthrough time.

479 As pointed out earlier from the analysis of the integrated temporal profiles, there are
480 significant differences in the shape and spreading between the two tracer compounds. At
481 lower Péclet number ($v \approx 0.5$ m/day), the shape of a particular compound's plume tend to
482 be less elongated (left column; Figure 4); whereas with the increasing seepage velocity (v
483 $\approx$ 5 and 25 m/day), the plume becomes more stretched along the longitudinal/time axis
484 (middle and right columns in Figure 5). This is expected since at high flow velocity, the

small characteristic advective time does not allow enough time for diffusion to act. This limits the macroscopic transverse displacement of the tracer plume, and at the pore scale, it results in incomplete mixing in the pore channels in highly advection-dominated systems.

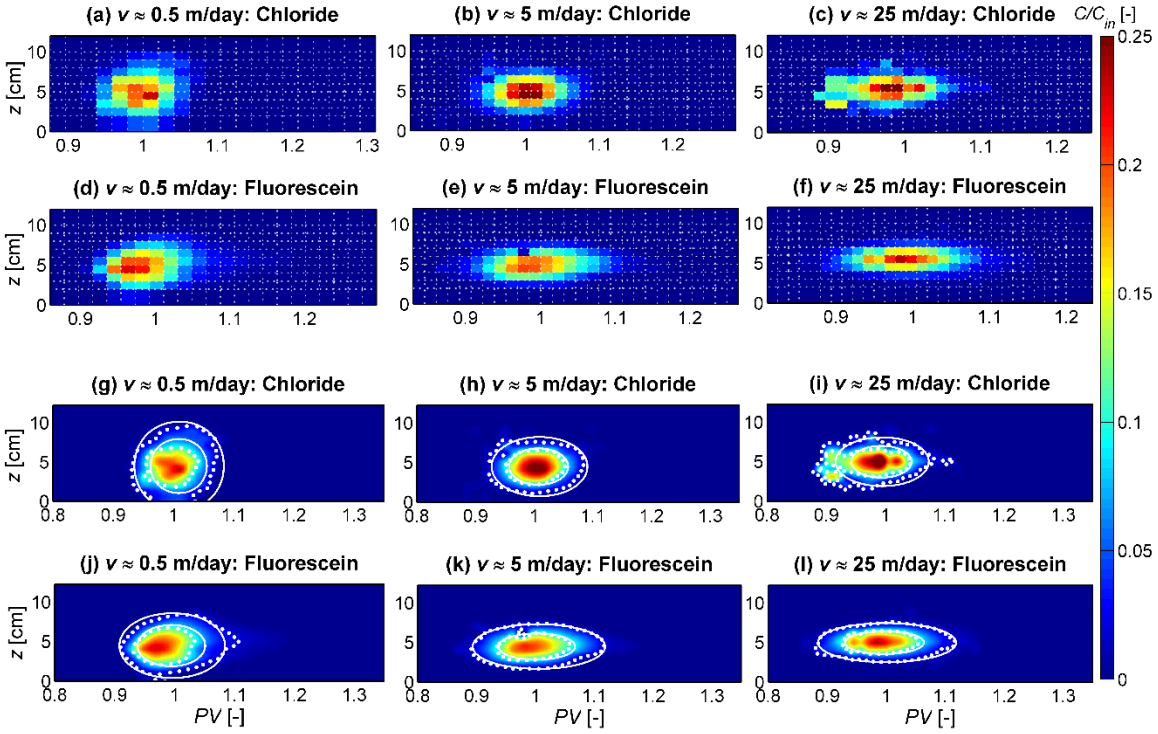

Figure 5: 2-D maps of concentration measurements performed at each individual outlet port as a function of time for different flow velocities: measured data points (a-f), and cubic interpolation of the measured values (g-l). The contour lines are shown for normalized concentration values of 0.02 and 0.1 with dots representing the interpolated measured values and the solid lines being the ADE predicted values.

It is interesting to note that fluorescein (Figure 5d-f,j-l) has a much longer and stretched plume compared to chloride (Figure 5a-c,g-i) at all flow velocities. This implies that following the simultaneous injection (with same initial size and shape), the tracer compounds undergo significantly different extents of spreading and mixing. These differences are attributed to their diffusive mobilites because both tracers are

simultaneously transported under identical hydraulic and transport conditions and through the same pore network. Such behavior is remarkable and confirms that the compound-specific effect does not vanish even at high pore-water velocities and can lead to significant differences in multispecies transport.

Figure 6 summarizes the breakthrough curves measured at different vertical locations (z) for the specific case of $v \approx 5$ m/day. The profiles measured at the central outlet ports of the vertical cross-section correspond to the core of the plumes and look similar to the integrated profiles of Figure 2 (Figure 6c-f). At the top and bottom locations (i.e., plume fringe area), the differences between the peak concentrations of the two tracer compounds tend to increase (Figure 6a-b,g-i). Such discrepancies arise from the differences in diffusion coefficients; where the higher D_{aq} of chloride leads to further transverse displacement. Hence, considerably higher peak concentrations of chloride are observed in the upper and lower plume fringe compared to the ones of fluorescein (Figure 6a,i). The measured data were fitted with the different transport models (ADE, CTRW and DDMT) for all locally measured profiles. In each port, the fitting was performed as 1-D transport problem (equation (2)) by considering the transport occurring along a streamtube from the point of injection to the point of observation (i.e., as if we consider each streamtube as an independent 1-D column).

It is important to mention that, the fitted longitudinal dispersion (D_L) values determined in different vertical locations show variability for both tracers (listed in Table S4). While the central ports show values similar to the one obtained from the integrated profiles, D_L has a decreasing trend especially from the core to the fringe of the plume. Also notice that at the outer fringe the quality of the fits decreases due to the considerably lower

values and more scattered patterns of measured concentrations. Fluorescein plumes typically show a higher dispersion coefficient, indicating more spreading along the streamtube (Table S4).

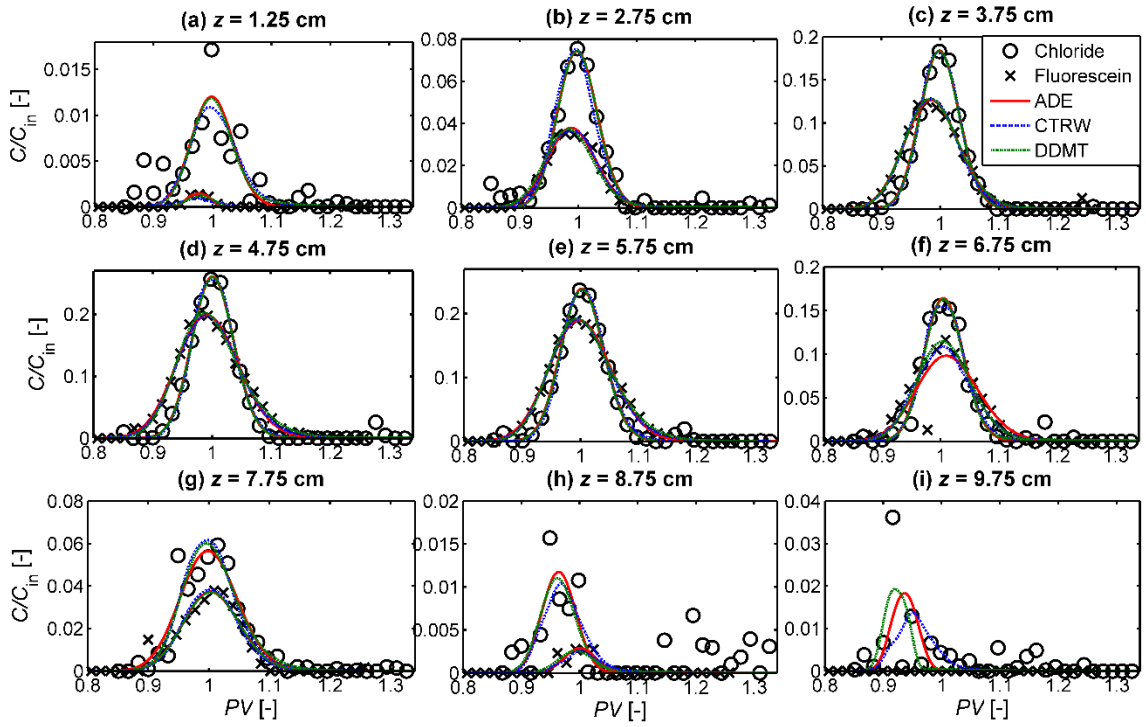

Figure 6. Breakthrough curves measured at each individual port for the seepage velocity of 5 m/day.

The calculated values of average seepage velocities (v) in each port are also consistent with the measured flow rates in the respective port. The degrees of anomalous behavior of chloride and fluorescein, interpreted based on the outcomes of the CTRW fits, are in a similar range as obtained from their integrated profiles. For chloride, β = 2.004 – 2.015 was found for different locations of the plume; whereas the fitted β for fluorescein stayed slightly below 2 (1.849 – 1.989) indicating the existence of "weak" non-Fickian behavior. The DDMT model fitting also suggest similar outcomes, as obtained from the CTRW model.

4.1.3 Transverse Spreading and Dispersion

We analyze the transverse displacement of the tracer plumes by integrating the concentration measurements along the time axis (equation (9)). This temporal integration, basically, determines the fraction of total injected tracer mass (zeroth temporal moments) recovered at each outlet port. In particular, with this approach, we eliminate the longitudinal plume evolution/spreading by disregarding any concentration gradient along each advective travel path of our 2-D domain. Consequently, the transport of the 2-D tracer pulse reduces to a more simplified form, which describes only the lateral concentration distribution in different longitudinal cross-sections. As explained in Section 3.2, these time-integrated vertical concentration profiles normalized by the temporal integral of the inflow boundary condition $\left(\hat{C}(x,z)\Big|_{BN}^{SP}\right)$ agree very well with the 2-D steady-state analytical solution of equation (10). We quantify the transverse dispersion coefficient (D_T) of different tracers by fitting equation (10) to the measurements by using the seepage velocities obtained from the integrated breakthrough profiles. For simplicity, we only fit the ADE model here to obtain the extent of transverse displacement.

Figure 7 represents the time-integrated spatial profiles for different cases at the end of our experimental domain. It is interesting to notice that the spreading and peak concentrations of the two tracers show a completely opposite behavior compared to the observations for the integrated breakthrough curves (Figure 2). In fact, in the lateral direction, the compound-specific behavior is more intuitive to interpret: chloride, the tracer with higher D_{aq}, has more spread profiles with lower peak concentrations compared to the ones of fluorescein (lower D_{aq}). Even in the case of strongly advection-dominated transport ($v \approx$ 25 m/day, Figure 7c), the compound-specific migration is significant and a considerable

separation between the two tracer profiles exists. Therefore, as pointed out from the analysis of the flux-related dilution index profiles for the integrated breakthrough curves (Figure 2d-f) and in the 2-D mapping of the plumes from the outlet measurements (Figure 5), the more diluted chloride plume shows more significant lateral displacement at all flow velocities.

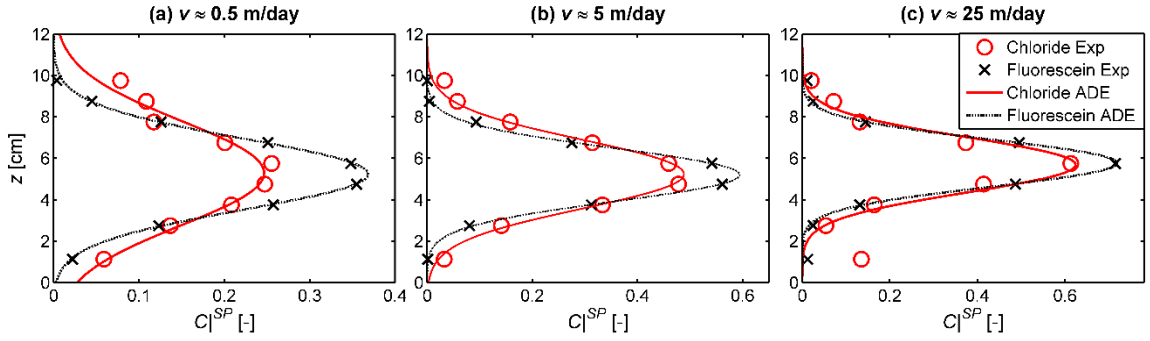

Figure 7. Time-integrated transverse concentration profiles, normalized by the temporal integral of the inflow boundary condition, for the seepage velocities of 0.5 (a), 5 (b), and 25 (c) m/day.

The fitted transverse dispersion coefficients (D_T) listed in Table 3 also show that the less mobile fluorescein has always a smaller value compared to chloride for all flow velocities. These D_T values are in very good agreement with the predictions from a non-linear compound-specific transverse dispersion parameterization (Figure 8). Such parameterization was inspired by an earlier statistical model of *Bear and Bachmat* [1967] and was developed based on steady-state flow-through experiments in the works of *Chiogna et al*. [2010] and *Rolle et al*. [2012]. The parameterization reads as:

$$D_T = D_P + D_{aq}\left(\frac{Pe^2}{Pe + 2 + 4\delta^2}\right)^B \qquad (18)$$

where D_P [L^2/T] is the pore diffusion coefficient; Pe [-] denotes the grain Péclet number, defined as $Pe = vd/D_{aq}$ (d [L] is the average grain size diameter); δ [-] is the ratio between

the length of a pore channel to its hydraulic radius; and B [-] is an empirical exponent accounting for incomplete mixing in pore channels. Notice that, in order to avoid confusions with β in CTRW interpretations, we use a capital beta (B) in equation (18). The values δ and B were characterized by conducting a series of multi-tracer laboratory and pore-scale experiments across a wide range of flow velocity and in porous media with different grain sizes [*Rolle et al.*, 2012; *Hochstelter et al.*, 2013; *Ye et al.*, 2015a; 2015b]. In our calculations we use $\delta = 6.2$ and B = 0.5, which are representative for the porous medium used in this study.

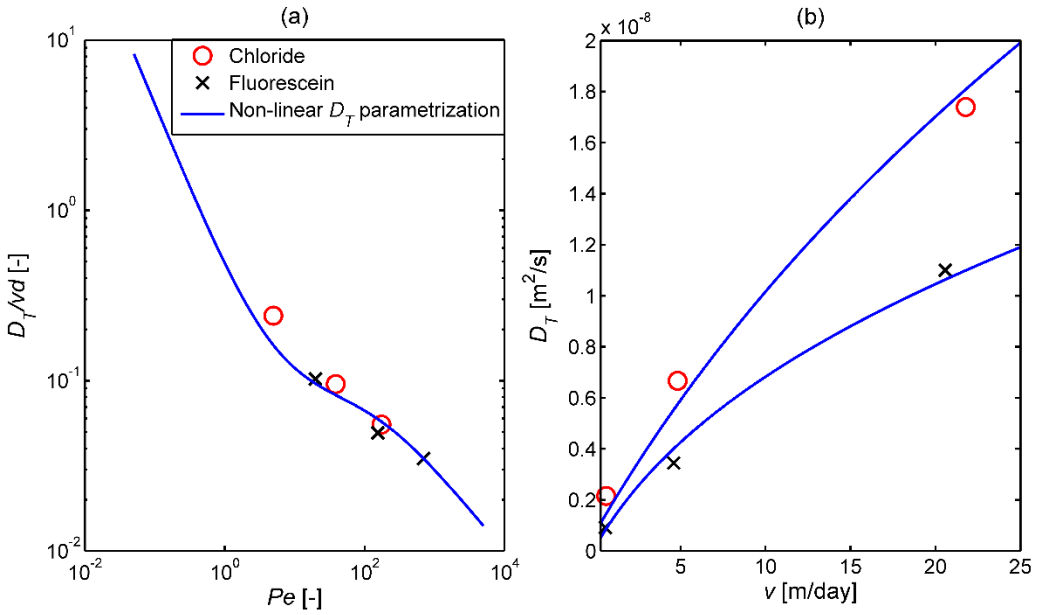

Figure 8. Comparison between the D_T values computed from the measurements performed in this study (markers) and the predictions from the non-linear compound-specific parameterization, equation 18, (lines).

Figure 8a directly compares the experimentally determined D_T values (markers) with the computed ones according to equation (18) (continuous line) as a function of *Pe*; whereas Figure 8b illustrates the pattern of D_T as a function of the seepage velocity, *v*. It is remarkable to notice that the compound-specific effects on transverse dispersion are also

598 relevant at high advective velocities, including at $v \approx 25$ m/day (Figure 8b). In fact, the
599 separation between the two tracer dispersion coefficients has an increasing trend with
600 increasing seepage velocities. Equation (18) captures this behavior by considering an
601 explicit dependence of the mechanical dispersion term on the aqueous diffusion
602 coefficients. Notice that, at the upper limit of our experimental seepage velocities ($v \approx 25$
603 m/day), the mechanical dispersion term is almost two orders of magnitudes higher
604 relative to the pore diffusion term. Therefore, the transient multitracer experiments
605 performed in this study confirm the importance of considering the dependence of
606 mechanical dispersion on both flow-velocity and species diffusivity, which was
607 previously experimentally investigated only under steady-state conditions and
608 considering continuous injection [*Chiogna et al*., 2010; *Rolle et al*., 2012].
609
610 **4.2 Multicomponent Ionic Experiments**
611 As summarized in Table 2, experiments were also performed to identify the impact of
612 Coulombic interactions during transient multicomponent ionic transport. Focusing on
613 different settings of ionic tracers, we consider two distinct experiments, in which the first
614 one includes the injection of a pulse of a 1:2 electrolyte ($MgCl_2$; 0.8 mM) solution in pure
615 water. The second experiment was performed by injecting the same electrolyte solution
616 ($MgCl_2$; 0.8 mM) but, this time, a NaBr solution (1:1 electrolyte; 4.04 mM) was used as
617 the background solution. As done in the multi-tracer cases illustrated in the previous
618 sections, the concentration measurements were performed at different outlet ports and at
619 different times. Both multicomponent ionic transport experiments were performed at a

620 seepage velocity of ≈ 5 m/day, which is still representative of strongly advection-
621 dominated regimes.
622 Figure 9 summarizes the spatially-integrated breakthrough curves as well as the time-
623 integrated transverse profiles for the two cases of multicomponent ionic transport. The
624 general shapes of these profiles are similar to the ones obtained for the multi-tracer
625 experiments (Figure 2 and 7). Notice that, although the same electrolyte species was used
626 as tracer in both experiments, the measured concentration profiles of the cation and the
627 anion are significantly different because of the different background solutions. For the
628 transport in pure water, Mg^{2+} and Cl^- plumes tend to travel together as indicated by their
629 practically identical temporal and spatial profiles despite the two have distinct diffusion
630 coefficients (Table 1; Figure 9a-b). Since pure water (Milli-Q) is free of any major ions,
631 the transported cation (Mg^{2+}) and anion (Cl^-) are electrostatically forced to travel together
632 in order to fulfill the charge balance of the system. In this case, the electromigration term
633 (equations (13) and (15)) will provide a positive contribution and "speed up" the
634 displacement of the less mobile cation (Mg^{2+}) and a negative contribution, slowing down
635 the displacement of the more mobile anion (Cl^-). The hydrodynamic dispersion
636 coefficients (D_L, D_T) obtained by fitting the measured profiles for these two cases with
637 the 1-D ADE model also provide very similar values for the two ions (for Mg^{2+}:
638 D_L=4.33×10^{-8}; D_T=5.55×10^{-9} and for Cl^-: D_L=4.13×10^{-8}; D_T=5.55×10^{-9} m^2/s).
639 In contrast, when $MgCl_2$ is injected in a NaBr background solution (with ~fivefold of the
640 injected tracer concentration), the system is already charge-balanced by the background
641 ions (Na^+ and Br^-). Hence, the plume ions (Mg^{2+} and Cl^-) can migrate with mobilities
642 close to their "self-diffusive/dispersive" properties without experiencing any noticeable

electrostatic interaction. Thus, distinct profiles of the concentrations of these ions were measured at the outlet of the flow-through setup (Figure 9c-d). Fitting these profiles also resulted in distinct values of longitudinal and transverse hydrodynamic dispersion coefficients D_L (for Mg^{2+}: D_L=6.05×10^{-8}; D_T=4.20×10^{-9} m^2/s and for Cl^-: D_L=3.78×10^{-8}; D_T=6.48×10^{-9} m^2/s).

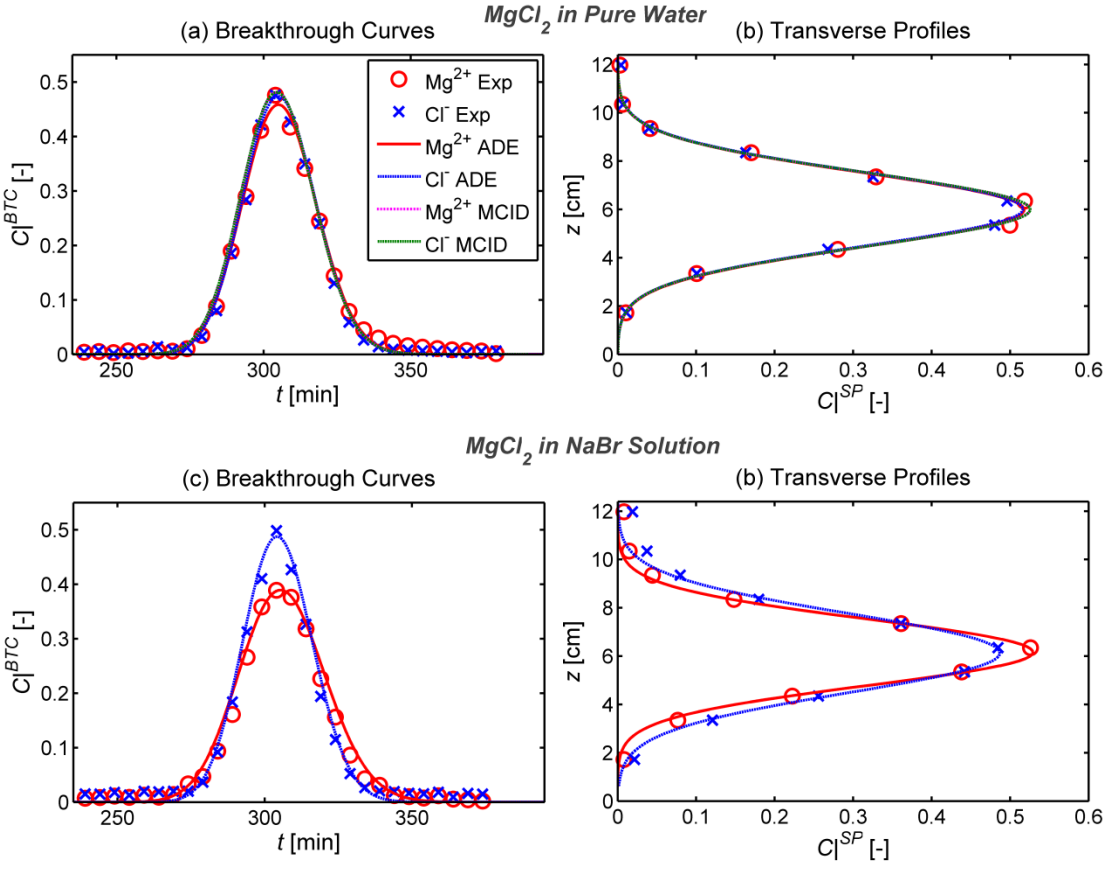

Figure 9. Integrated breakthrough curves (a,c) and vertical concentration profiles (b,d) during transport of $MgCl_2$ in pure water (a-b) and in NaBr background solution (c-d). The markers indicate the measured quantities whereas the lines represent the fitted profiles with 1-D ADE model (solid lines) and the simulated profiles with the 2-D multicomponent ionic transport model (dotted lines).

Notice that in the second multicomponent ionic experiment, in which both longitudinal and transverse profiles became distinct, the same patterns discussed in the previous

sections were observed: more peaked and less spread breakthrough curves for the more mobile species (in this cases Cl^-), which, instead, show a more spread and less peaked profile in the lateral direction compared to the less mobile ion (Mg^{2+}). Although, accurately capturing transport processes of these ionic species requires either a detailed pore-scale model or a continuum model, with correct dispersion parameterizations (both longitudinal and transverse) accounting for all the relevant processes (e.g., species diffusion, flow-velocity, and the extent of incomplete mixing in the pores), here we attempt to predict the multicomponent transport of $MgCl_2$ in pure water by using the overall dispersion parameters obtained from the case of transport in buffer electrolyte (NaBr). This treatment is based on the assumption that in the presence of NaBr background solution, Mg^{2+} and Cl^- travel exactly according to their self-diffusivities (i.e., as if charge-neutral species). Therefore, the values of D_L and D_T of these ions obtained from this case can be regarded as their "self-dispersion" coefficients. We considered these fitted "bulk dispersion" values as input parameters for the multicomponent ionic dispersion model (equation (17); Section 3.4) to predict the coupled transport of $MgCl_2$ in pure water. The magenta and green dotted lines in Figure 9a-b refer to the predicted concentration profiles from the 2-D multicomponent ionic transport simulations, which show a very good agreement with the measurements and the fitted 1-D profiles.

The 2-D multicomponent ionic transport model enables us to effectively visualize the electrostatic interactions by mapping the spatial distributions of different flux components (equation (13): $J_{tot} = J_{dis} + J_{mig}$). In Figure 10, we illustrate the behavior for the case of transport of $MgCl_2$ in pure water. The top two rows represent the longitudinal flux components (Figure 10a-f), whereas the remaining bottom panels refer to the

transverse flux components (Figure 10g-l) after t = 50, 150, and 250 minutes of simulation.

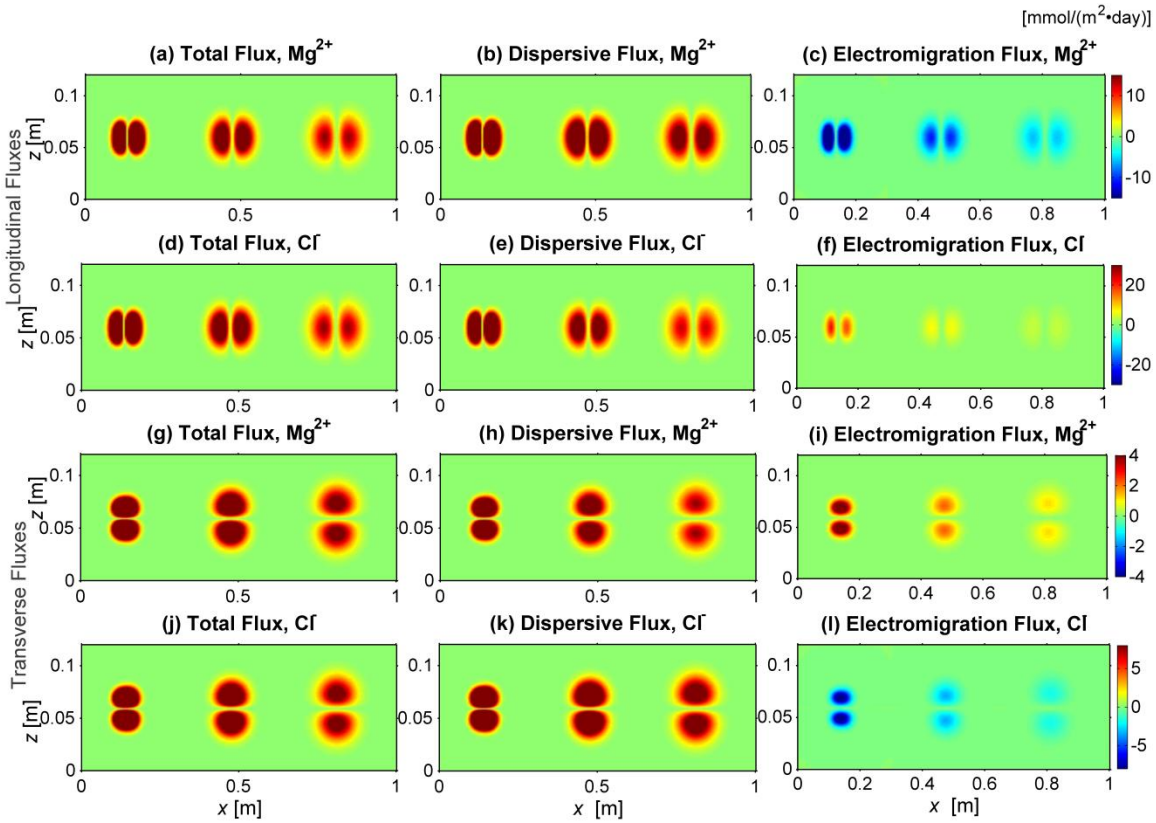

Figure 10. Maps of multicomponent ionic flux components in the longitudinal (a-f) and transverse (g-i) direction for the transport of $MgCl_2$ in pure water after t = 50, 150, and 250 minutes. The direction from the core to the fringe of the plume is considered positive in the flux calculations.

It is interesting to notice that, although both Mg^{2+} and Cl^- have identical overall distributions of total fluxes (J_{tot}) (left column panels), the different components of J_{tot} are distinct because of the variation in the "self-dispersion" coefficients of the different species. For transverse fluxes, J_{dis} values are higher for Cl^- compared to Mg^{2+}, since Cl^- has higher D_T (Figure 10h and 10k). The situation is opposite in the longitudinal J_{dis} distributions where Mg^{2+} apparently has a macroscopically higher D_L (Figure 10b and

694 10e). The electrochemical migration flux components, J_{mig} have the most interesting
695 distributions with the cation (Mg^{2+}) and anion (Cl^{-}) species showing similar pattern but
696 opposite signs (right column panels). Such negative correlation facilitates an
697 enhancement in the total flux for the less mobile species, and a reduction for the more
698 mobile species, respectively. Thus, the electrostatic potential gradient couples the
699 positively and negatively charged species leading to practically identical concentration
700 profiles.
701
702
703 **5. CONCLUSIONS**
704 The high-resolution flow-through experiments performed in this study provides first
705 experimental evidence of compound-specific diffusion/dispersion effects, as well as
706 Coulombic interactions during multispecies transient transport in porous media, under
707 advection-dominated conditions.
708 Furthermore, both the experimental and the simulation outcomes show that non-Fickian
709 or "anomalous" transport, highlighting the impact of unresolved pore-scale heterogeneity,
710 is observed in most cases even though the experimental domain was macroscopically
711 "homogeneous". Our experiments also show that the sole analysis of integrated
712 breakthrough curves may not provide an adequate portrayal of actual transport processes
713 and can even lead to erroneous conclusions regarding mixing and plume dilution,
714 especially under high flow velocities. We also show that experimentally-determined
715 entropy-based metrics, such as the flux-related dilution index, are useful to help
716 distinguishing plume spreading from mixing.

717 The results of our experiments clearly highlight the importance of diffusion and
718 electrochemical interactions on macroscopic solute transport. Perhaps due to the
719 perception of the small scale at which these processes occur and/or the small numerical
720 values of the related coefficients, the study of these phenomena in advection-dominated
721 flow-through systems has received only limited attention. Our results show that small-
722 scale processes have an important influence on macroscopic transport behavior in porous
723 media. These findings are relevant for advancing the understanding of solute transport in
724 groundwater, which is often, inherently, a multispecies (i.e., compound-specific) and/or a
725 multicomponent ionic transport problem (i.e., major ions and many dissolved
726 contaminants are charged species). In our view, the outcomes of these experiments
727 provide also a valuable dataset for the development of modeling approaches. In fact,
728 despite satisfactory results could be obtained by fitting different models to distinct
729 experiment data, comprehensive frameworks able to consistently represent the
730 macroscopic effects of small scale interactions through the different conditions of flow
731 velocity, compound-specific properties and electrostatic interaction need to be developed.
732 Our investigation was carried out considering conservative transport under simplified
733 physical and chemical conditions. The extrapolation of these outcomes to more complex
734 physically and chemically heterogeneous natural or engineered systems remains an open
735 challenge. Furthermore, these experiments were performed in quasi 2-D setups and it is
736 not clear, yet, how such effects will impact transient transport in fully 3-D domains, in
737 which the role of diffusion and compound-specific mixing is quantitatively more
738 significant [*Ye al*., 2015b], but also more complex flow topologies, resulting from
739 physical heterogeneity and/or anisotropy [*Ye et al*., 2015c; *Chiogna et al*., 2014; *Cirpka*

740 *et al.*, 2015], may affect the behavior and magnitude of mixing as well as electrochemical
741 migration. The expected increase in the availability of high-resolution investigations at
742 different scales from microfluidic experiments [e.g., *Zhang et al*., 2010; *De Anna et al*.,
743 2014], to laboratory (as the present study) and field-scale [e.g. *Tuxen et al., 2006;*
744 *Prommer et al*., 2009], will provide unprecedented capabilities to understand and
745 quantify small scale subsurface processes. Furthermore, enhanced possibilities to resolve
746 the small scale will lead to significant improvement in describing and properly upscaling
747 the effects of diffusion and electromigration processes in multispecies, macroscopic
748 transport in porous media.
749

750 **Acknowledgments**

751 The experimental data for the concentration breakthrough measurements at the outlet of
752 the flow-through setup are provided in the Supporting Information for the multi-tracer
753 experiments (Table S2) and the multicomponent ionic experiments (Table S3). The
754 description of the different model formulations used in this study is also presented in the
755 Supporting Information (Section S1). The document also provides the comparison of the
756 simplified 1-D integrated breakthrough curves and vertical profiles with a 2-D analytical
757 solution.
758 The authors thank Jens Schaarup Sørensen for the assistance in establishing the
759 experimental setup and the ion-chromatography measurements. We also thank Sinh Hy
760 Nguyen and Mikael Emil Olsson for performing the ICP-MS measurements.
761 M.R. and M.M. acknowledge the Baden-Württemberg Stiftung for the financial support
762 of this research project by the Eliteprogram for Postdocs.
763
764
765

References

Appelo, C. A. J., and P. Wersin (2007), Multicomponent diffusion modeling in clay systems with application to the diffusion of tritium, iodide, and sodium in opalinus clay, *Environ. Sci. Technol.*, *41*(14), 5002-5007.

Appelo, C. A. J., A. Vinsot, S. Mettler, and S. Wechner (2008), Obtaining the porewater composition of a clay rock by modeling the in- and out-diffusion of anions and cations from an in-situ experiment, *J. Contam. Hydrol.*, *101*(1-4), 67-76.

Bard, A. J., and L. R. Faulkner (2001), *Electrochemical Methods: Fundamentals and Applications*, second ed., 833 pp., John Wiley, New York.

Bear, J. (1972), *Dynamics of Fluids in Porous Media*, 764 pp., American Elsevier Pub. Co., New York.

Ben-Yaakov, S. (1972), Diffusion of sea water ions—I. Diffusion of sea water into a dilute solution, *Geochim. Cosmochim. Acta*, *36*(12), 1395-1406.

Berkowitz, B., and H. Scher (2009), Exploring the nature of non-Fickian transport in laboratory experiments, *Adv. Water Resour.*, *32*(5), 750-755.

Berkowitz, B., A. Cortis, M. Dentz, and H. Scher (2006), Modeling non-Fickian transport in geological formations as a continuous time random walk, *Rev. Geophys.*, *44*(2), RG2003, doi:10.1029/2005RG000178.

Bijeljic, B., A. H. Muggeridge, and M. J. Blunt (2004), Pore-scale modeling of longitudinal dispersion, *Water Resour. Res.*, *40*, W11501, doi:10.1029/2004WR003567.

Boudreau, B. P. (1997), *Diagenetic Models and Their Implementation: Modelling Transport And Reactions In Aquatic Sediments*, 414 pp., Springer-Verlag, Heidelberg.

Boudreau, B. P., F. J. R. Meysman, and J. J. Middelburg (2004), Multicomponent ionic diffusion in porewaters: Coulombic effects revisited, *Earth Planet. Sci. Lett.*, *222*(2), 653-666.

Cao, J., and P. K. Kitanidis (1998), Pore-scale dilution of conservative solutes: An example, *Water Resour. Res.*, *34*(8), 1941–1949, doi:10.1029/98WR01468.

Carrera, J., X. Sanchez-Vila, I. Benet, A. Medina, G. Galarza, and J. Guimera (1998), On matrix diffusion: formulations, solution methods and qualitative effects, *Hydrogeol. J*, *6*(1), 178-190.

Chiogna, G., and A. Bellin (2013), Analytical solution for reactive solute transport considering incomplete mixing within a reference elementary volume, *Water Resour. Res.*, 49, 2589–2600, doi:10.1002/wrcr.20200.

Chiogna, G., O. A. Cirpka, P. Grathwohl, and M. Rolle (2011), Relevance of local compound-specific transverse dispersion for conservative and reactive mixing in heterogeneous porous media, *Water Resour. Res.*, *47*(7), W07540.

Chiogna, G., M. Rolle, A. Bellin, and O. A. Cirpka (2014), Helicity and flow topology in three-dimensional anisotropic porous media, Adv. Water Resour., 73, 134-143.

Chiogna, G., C. Eberhardt, P. Grathwohl, O. A. Cirpka, and M. Rolle (2010), Evidence of compound-dependent hydrodynamic and mechanical transverse dispersion by multitracer laboratory experiments, *Environ. Sci. Technol.*, *44*(2), 688-693.

809 Cirpka, O. A., and P. K. Kitanidis (2000), An advective-dispersive stream tube approach
810 for the transfer of conservative-tracer data to reactive transport, *Water Resour.*
811 *Res.*, *36*(5), 1209-1220.
812 Cirpka, O. A., F. P. J. de Barros, G. Chiogna, M. Rolle, and W. Nowak (2011), Stochastic
813 flux‐related analysis of transverse mixing in two-dimensional heterogeneous
814 porous media, *Water Resour. Res.*, *47*, W06515, doi:10.1029/2010WR010279.
815 Cirpka, O. A., E. O. Frind, and R. Helmig (1999a), Numerical methods for reactive
816 transport on rectangular and streamline-oriented grids, *Adv. Water Resour.*, *22*(7),
817 711-728.
818 Cirpka, O. A., E. O. Frind, and R. Helmig (1999b), Streamline-oriented grid generation
819 for transport modelling in two-dimensional domains including wells, *Adv. Water*
820 *Resour.*, *22*(7), 697-710.
821 Cirpka, O. A., G. Chiogna, M. Rolle, and A. Bellin (2015), Transverse mixing in three-
822 dimensional nonstationary anisotropic heterogeneous porous media, *Water*
823 *Resour. Res.*, *51*(1), 241-260.
824 Coleman, T.F., Li, Y., 1996. An interior, trust region approach for nonlinear
825 minimization subject to bounds. *SIAM J. Optim. 6*, 418–445.
826 Cortis, A., and B. Berkowitz (2005), Computing "anomalous" contaminant transport in
827 porous media: The CTRW MATLAB Toolbox, *Ground Water*, *43*(6), 947-950.
828 Cussler, E. L. (2009), *Diffusion: Mass Transfer in Fluid Systems*, third ed., 631 pp.,
829 Cambridge University Press, Cambridge.
830 Davis, T., and I. Duff (1997), An unsymmetric-pattern multifrontal method for sparse LU
831 factorization, *SIAM Journal on Matrix Analysis and Applications*, 18(1), 140-158.
832 de Anna, P., J. Jimenez-Martinez, H. Tabuteau, R. Turuban, T. Le Borgne, M. Derrien,
833 and Y. Méheust (2014), Mixing and reaction kinetics in porous media: An
834 experimental pore scale quantification, *Environ. Sci. Technol.*, *48*, 508–516.
835 Delgado, J. M. P. Q. (2006), A critical review of dispersion in packed beds, *Heat Mass*
836 *Transfer.*, *42*(4), 279-310.
837 Dentz, M., T. Le Borgne, A. Englert, and B. Bijeljic (2011), Mixing, spreading and
838 reaction in heterogeneous media: A brief review, *J. Contam. Hydrol.*, 120–121,
839 1–17, doi:10.1016/j.jconhyd.2010.05.002.
840 Domenico, P. A., and V. V. Palciauskas (1982), Alternative boundaries in solid waste
841 management, *Ground Water*, *20*(3), 303-311.
842 Edery, Y., H. Sher, and B. Berkowitz (2009), Modeling bimolecular reactions and
843 transport in porous media, *Geophys. Res. Lett.*, *36*, L02407,
844 doi:10.1029/2008GL036381.
845 Felmy, A. R., and J. H. Weare (1991), Calculation of multicomponent ionic-diffusion
846 from zero to high-concentration I. The system Na-K-Ca-Mg-Cl-SO_4-H_2O at 25-
847 Degrees-C, *Geochim. Cosmochim. Acta*, *55*(1), 113-131.
848 Fiori, A., I. Jankovic, and G. Dagan (2011), The impact of local diffusion upon mass
849 arrival of a passive solute in transport through three-dimensional highly
850 heterogeneous aquifers, *Adv. Water Resour.*, *34*(12), 1563-1573.
851 Giambalvo, E. R., C. I. Steefel, A. T. Fisher, N. D. Rosenberg, and C. G. Wheat (2002),
852 Effect of fluid-sediment reaction on hydrothermal fluxes of major elements,
853 eastern flank of the Juan de Fuca Ridge, *Geochim. Cosmochim. Acta*, *66*(10),
854 1739-1757.

Gorelick, S. M., G. Liu, and C. Zheng (2005), Quantifying mass transfer in permeable media containing conductive dendritic networks, *Geophys. Res. Lett.*, *32*(18), L18402, doi:10.1029/2005GL023512.

Gramling, C. M., C. F. Harvey, and L. C. Meigs (2002), Reactive transport in porous media: A comparison of model prediction with laboratory visualization, *Environ. Sci. Technol.*, *36*(11), 2508–2514.

Guedes de Carvalho J. R. F., J. M. P. Q. Delgado (2005), Overall map and correlation of dispersion data for flow through granular packed beds, *Chem. Eng. Sci. 60*, 365-75. doi: http://dx.doi.org/10.1016/j.ces.2004.07.121

Gvirtzman, H., and S. M. Gorelick (1991), Dispersion and advection in unsaturated porous media enhanced by anion exclusion, *Nature*, *352*, 793–795.

Haberer, C. M., M. Rolle, S. Liu, O. A. Cirpka, and P. Grathwohl (2011), A high-resolution non-invasive approach to quantify oxygen transport across the capillary fringe and within the underlying groundwater, *J. Contam. Hydrol.*, *122*(1–4), 26-39.

Haberer, C. M., M. Rolle, O. A. Cirpka, and P. Grathwohl (2012), Oxygen transfer in a fluctuating capillary fringe, *Vadose Zone J.*, 11(3).

Hadley, P. W., and C. Newell (2014), The new potential for understanding groundwater contaminant transport, *Groundwater*, *52*(2), 174-186.

Haggerty, R., and S. M. Gorelick (1995), Multiple-rate mass-transfer for modeling diffusion and surface-reactions in media with pore-scale heterogeneity, *Water Resour. Res.*, *31*(10), 2383-2400.

Heidari, P., and L. Li (2014), Solute transport in low-heterogeneity sandboxes: The role of correlation length and permeability variance, *Water Resour. Res.*, *50*(10), 8240-8264.

Hochstetler, D. L., M. Rolle, G. Chiogna, C. M. Haberer, P. Grathwohl, and P. K. Kitanidis (2013), Effects of compound-specific transverse mixing on steady-state reactive plumes: Insights from pore-scale simulations and Darcy-scale experiments, *Adv. Water Resour.*, *54*, 1-10.

Kitanidis, P. K. (1994), The concept of the Dilution Index, *Water Resour. Res.*, *30*(7), 2011-2026.

Kosakowski, G., B. Berkowitz, and H. Scher (2001), Analysis of field observations of tracer transport in a fractured till, *J. Contam. Hydrol.*, *47*(1), 29–51, doi:10.1016/S0169-7722(00)00140-6.

LaBolle, E. M., and G. E. Fogg (2001), Role of molecular diffusion in contaminant migration and recovery in an alluvial aquifer system, *Transp. Porous Med.*, *42*(1-2), 155-179.

Lasaga, A. C. (1979), The treatment of multi-component diffusion and ion pairs in diagenetic fluxes, *Am. J. Sci.*, *279*(3), 324-346.

Lasaga, A. C. (1998), *Kinetic Theory in the Earth Sciences*, 811 pp., Princeton University Press, Princeton, N.J.

Le Borgne, T., M. Dentz, P. Davy, D. Bolster, J. Carrera, J. de Dreuzy, and O. Bour (2011), Persistence of incomplete mixing: A key to anomalous transport, *Phys. Rev. E*, *84*, 015,301.

900 Leij, F. J., T. H. Skaggs, and M. T. Van Genuchten (1991), Analytical solutions for solute
901 transport in three-dimensional semi-infinite porous media, *Water Resour. Res.*,
902 *27*(10), 2719-2733.
903 Liu, C. X. (2007), An ion diffusion model in semi-permeable clay materials, *Environ. Sci.*
904 *Technol.*, *41*(15), 5403-5409.
905 Liu, C. X., J. Shang, and J. M. Zachara (2011), Multispecies diffusion models: A study of
906 uranyl species diffusion, *Water Resour. Res.*, *47*, W12514,
907 doi:10.1029/2011WR010575.
908 Luo, J., M. Dentz, O. A. Cirpka, and P. K. Kitanidis (2007), Breakthrough curve tailing
909 in a dipole flow field, *Water Resour. Res.*, *43*(9), W09403,
910 doi:10.1029/2006WR005600.
911 Luo, J., O. A. Cirpka, W. Wu, M. N. Fienen, P. M. Jardine, T. L. Mehlhorn, D. B.
912 Watson, C. S. Criddle, and P. K. Kitanidis (2005), Mass-transfer limitations for
913 nitrate removal in a uranium-contaminated aquifer, *Environ. Sci. Technol.*,
914 *39*(21), 8453-8459.
915 Molins, S., D. Trebotich, C. I. Steefel, and C. P. Shen (2012), An investigation of the
916 effect of pore scale flow on average geochemical reaction rates using direct
917 numerical simulation, *Water Resour. Res.*, *48*. W03527.
918 http://dx.doi.org/10.1029/2011WR011404
919 Muniruzzaman, M., and M. Rolle (2015), Impact of multicomponent ionic transport on
920 pH fronts propagation in saturated porous media, *Water Resour. Res.*, *51*(8),
921 6739-6755.
922 Muniruzzaman, M., and M. Rolle (2016), Modeling multicomponent ionic transport in
923 groundwater with IPhreeqc coupling: Electrostatic interactions and geochemical
924 reactions in homogeneous and heterogeneous domains, *Adv. Water Resour.*, *98*, 1-
925 15. http://dx.doi.org/10.1016/j.advwatres.2016.10.013.
926 Muniruzzaman, M., C. M. Haberer, P. Grathwohl, and M. Rolle (2014), Multicomponent
927 ionic dispersion during transport of electrolytes in heterogeneous porous media:
928 Experiments and model-based interpretation, *Geochim. Cosmochim. Acta*, *141*(0),
929 656-669.
930 Porta, G. M., B. Bijeljic, M. J. Blunt, and A. Guadagnini (2015), Continuum-scale
931 characterization of solute transport based on pore-scale velocity distributions,
932 *Geophys. Res. Lett.*, *42*, 7537–7545, doi:10.1002/2015GL065423.
933 Prommer, H., B. Anneser, M. Rolle, F. Einsiedl, and C. Griebler, (2009), Biogeochemical
934 and isotopic gradients in a BTEX/PAH contaminant plume: Model-based
935 interpretation of a high-resolution field data set, *Environ. Sci. Technol.*, *43*, 8206–
936 8212, doi:10.1021/es901142a
937 Raje, D. S., and V. Kapoor (2000), Experimental study of bimolecular reaction kinetics in
938 porous media, *Environ. Sci. Technol.*, *34*, 1234–1239, doi:10.1021/es9908669
939 Rolle, M., and P. K. Kitanidis (2014), Effects of compound-specific dilution on transient
940 transport and solute breakthrough: A pore-scale analysis, *Adv. Water Resour.*, *71*,
941 186-199.
942 Rolle, M., G. Chiogna, D. L. Hochstetler, and P. K. Kitanidis (2013a), On the importance
943 of diffusion and compound-specific mixing for groundwater transport: An
944 investigation from pore to field scale, *J. Contam. Hydrol.*, *153*(0), 51-68.

945 Rolle, M., M. Muniruzzaman, C. M. Haberer, and P. Grathwohl (2013b), Coulombic
946 effects in advection-dominated transport of electrolytes in porous media:
947 Multicomponent ionic dispersion, *Geochim. Cosmochim. Acta, 120*(0), 195-205.
948 Rolle, M., C. Eberhardt, G. Chiogna, O. A. Cirpka, and P. Grathwohl (2009),
949 Enhancement of dilution and transverse reactive mixing in porous media:
950 Experiments and model-based interpretation, *J. Contam. Hydrol., 110*(3–4), 130-
951 142.
952 Rolle, M., D. L. Hochstetler, G. Chiogna, P. K. Kitanidis, and P. Grathwohl (2012),
953 Experimental investigation and pore-scale modeling interpretation of compound-
954 specific transverse dispersion in porous media, *Transp. Porous Med., 93*(3), 347-
955 362.
956 Sanchez-Vila, X., D. Fernàndez-Garcia, and A. Guadagnini (2010), Interpretation of
957 column experiments of transport of solutes undergoing an irreversible bimolecular
958 reaction using a continuum approximation, *Water Resour. Res., 46*, W12510,
959 doi:10.1029/2010WR009539
960 Scheidegger, A. E. (1961), General theory of dispersion in porous media, *J. Geophys.*
961 *Res., 66*(10), 3273-3278.
962 Scheven, U. M. (2013), Pore-scale mixing and transverse dispersivity of randomly
963 packed monodisperse spheres, *Phys. Rev. E, 110*(21), 214504. doi:
964 10.1103/PhysRevLett.110.214504
965 Steefel, C. I., and K. Maher (2009), Fluid-rock interaction: A reactive transport approach,
966 *Rev. Mineral. Geochem., 70*, 485-532.
967 Tartakovsky, A. M., G. D. Tartakovsky, and T. D. Scheibe (2009), Effects of incomplete
968 mixing on multicomponent reactive transport, *Adv. Water Resour., 32*(11), 1674–
969 1679, doi:10.1016/j.advwatres.2009.08.012.
970 Thullner, M., P. Van Cappellen, and P. Regnier (2005), Modeling the impact of microbial
971 activity on redox dynamics in porous media, *Geochim. Cosmochim. Acta, 69*(21),
972 5005-5019.
973 Tuxen N., H.J. Albrechtsen, and P.L. Bjerg (2006), Identification of a reactive
974 degradation zone at a landfill leachate plume fringe using high-resolution
975 sampling and incubation techniques. *J. Contam. Hydrol.*, 85, 179-194.
976 Valocchi, A. J. (1985), Validity of the local equilibrium assumption for modeling sorbing
977 solute transport through homogeneous soils, *Water Resour. Res., 21*(6), 808-820.
978 Van Cappellen, P., and J.-F. Gaillard (1996), Biogeochemical dynamics in aquatic
979 sediments, *Rev. Mineral. Geochem., 34*(1), 335-376.
980 van Genuchten, M. T., and P. J. Wierenga (1976), Mass transfer studies in sorbing porous
981 media I. Analytical solutions 1, *Soil Sci. Soc. Am. J., 40*(4), 473-480.
982 van Genuchten, M. T., F. J. Leij, T. H. Skaggs, N. Toride, S. A. Bradford, and E. M.
983 Pontedeiro (2013), Exact analytical solutions for contaminant transport in rivers 1.
984 The equilibrium advection-dispersion equation, *J. Hydrol. Hydromech., 61*(2),
985 146-160.
986 Vinograd, J. R., and J. W. McBain (1941), Diffusion of electrolytes and of the ions in
987 their mixtures, *J. Am. Chem. Soc., 63*(7), 2008-2015.
988 Wang, Y. F., and P. VanCappellen (1996), A multicomponent reactive transport model of
989 early diagenesis: Application to redox cycling in coastal marine sediments,
990 *Geochim. Cosmochim. Acta, 60*(16), 2993-3014.

991 Willmann, M., J. Carrera, and X. Sanchez-Vila (2008), Transport upscaling in
992 heterogeneous aquifers: What physical parameters control memory functions?,
993 *Water Resour. Res.*, *44*, W12437, doi:10.1029/2007WR006531.
994 Worch, E. (1993), A new equation for the calculation of diffusion coefficients for
995 dissolved substances, *Vom Wasser*, *81*, 289–297.
996 Ye, Y., G. Chiogna, O. A. Cirpka, P. Grathwohl, and M. Rolle (2015b), Experimental
997 evidence of helical flow in porous media, *Phys. Rev. Lett.*, *115*(19), 194502.
998 Ye, Y., G. Chiogna, O. Cirpka, P. Grathwohl, and M. Rolle (2015a), Experimental
999 investigation of compound-specific dilution of solute plumes in saturated porous
1000 media: 2-D vs. 3-D flow-through systems, *J. Contam. Hydrol.*, *172*, 33-47.
1001 Ye, Y., G. Chiogna, O. A. Cirpka, P. Grathwohl, and M. Rolle (2015c), Enhancement of
1002 plume dilution in two-dimensional and three-dimensional porous media by flow
1003 focusing in high-permeability inclusions, *Water Resour. Res.*, *51*(7), 5582-5602.
1004 Zhang, C. Y., K. Dehoff, N. Hess, M. Oostrom, T. W. Wietsma, A. J. Valocchi, B. W.
1005 Fouke, and C. J. Werth (2010), Pore-scale study of transverse mixing induced
1006 caco3 precipitation and permeability reduction in a model subsurface sedimentary
1007 system, *Environ. Sci. Technol.*, *44*(20), 7833-7838.
1008